

CARMApy: An Open-Source Python Framework for Simulating Microphysical Clouds in Planetary Atmospheres

WOLF CUKIER ¹, DIANA POWELL ¹, XI ZHANG ², PETER GAO ³, DOMINIC SAMRA ¹ AND VIGHNESH NAGPAL ^{1,*}

¹*Department of Astronomy & Astrophysics, the University of Chicago, Chicago, IL, 60637, USA*

²*Department of Earth and Planetary Sciences, University of California Santa Cruz, Santa Cruz, CA, 95064, USA*

³*Earth and Planets Laboratory, Carnegie Institution for Science, Washington, DC, USA*

ABSTRACT

CARMApy is a new open-source python code that performs bin-scheme microphysical modeling of clouds in exoplanet atmospheres. It models key cloud properties such as particle size distributions and microphysical rates from first principles. The code is a wrapper of ExoCARMA, a well tested Fortran code with an almost half century long heritage. CARMApy includes the microphysical processes of homogeneous and heterogeneous nucleation, condensational growth, evaporation, coagulation, and vertical transport. CARMApy has 10 built-in default condensates and allows the user to specify additional condensates. In this work we describe CARMApy and the data products that it can generate, along with the history of its code heritage. We additionally compile a complete description of the theory and methods used in CARMA. Lastly we benchmark CARMApy and show that its results are consistent with previous versions of CARMA, while executing the code ~ 1.9 times faster single threaded ~ 3.8 times faster multithreaded.

Keywords: Atmospheric clouds (2180), Planetary science (1255), Exoplanet atmospheres (487), Open source software (1866), Astronomy software (1855)

1. INTRODUCTION

Clouds impart first order impacts on planetary atmospheric properties and our interpretations thereof. Uncertainties in cloud formation processes can propagate to substantial uncertainties in inferences of atmospheric composition (eg. C/O (C. Helling et al. 2016), Mg/Si (E. Calamari et al. 2024)), atmospheric and interior P-T structure (e.g., P. Mollière et al. 2020), and atmospheric dynamics. For example, cloud formation is sensitive to atmospheric structure and mixing in the deep atmosphere which is otherwise unobservable (D. Powell et al. 2018) and the locations of clouds in atmospheres is one of our best probes of the atmospheric dynamics on these bodies (eg. L. Di Girolamo et al. 2025; M. K. Plummer et al. 2025). Clouds and radiative transfer are strongly coupled (V. Parmentier et al. 2021) and clouds are needed to understand planetary energy budgets (I. Malsky et al. 2024). The exact way which clouds shape these observations is determined by a number of key cloud properties such as the precise 3-D distribution of clouds on these bodies, the particle size distributions of clouds in each of these locations, the composition of the cloud particles, the shapes of the cloud particles, how all of these properties vary over time and how all these properties effect the optical properties of the cloud particles.

The field has employed models of clouds across a variety of levels of complexity that capture different amounts of these key properties. On the simple end of this spectrum exist gray cloud (GC) models. GC models assume a cloud deck with constant transmittance across all wavelengths, making them incredibly efficient and thus widely used in retrieval studies of exoplanet atmospheres (eg. Q. Xue et al. 2024). GC models make an extreme tradeoff prioritizing efficiency over capturing the physical complexities of clouds. Equilibrium cloud condensation (ECC) models (A. S. Ackerman & M. S. Marley 2001) are a class of commonly used models for exoplanetary clouds that exist a step up the complexity ladder from GC models (eg. M. S. Marley et al. 2021; C. V. Morley et al. 2024). ECC models, as their name implies, assume equilibrium behavior in the atmosphere—they assume that supersaturated gasses will

condense out of the atmosphere, forming clouds, until the gas reaches a saturation ratio of unity. ECC modeling frameworks are fast to run, making them well suited to tasks such as 1-D models that solve for the radiative state of an atmosphere. These models, however, require a prescribed shape for the cloud particle size distribution and involve a fitted parameter (known as f_{sed}) with unclear physical meaning, obscuring the physical processes that might be forming these clouds. Moment-method kinetic cloud (MMKC) formation models (P. Woitke & C. Helling 2003, 2004) are also used to model clouds on planetary objects which fold even in more physics—MMKC models are highly detailed and include built-in chemistry calculations. Similar to the ECC models, however, these models still require a prescribed functional form for the particle size distribution (E. K. H. Lee & K. Ohno 2025a). While all of these models have their individual strengths, inability of these models to resolve arbitrary cloud particle size distributions leads them to struggle to reproduce both certain observed spectral features and bulk properties in these bodies, especially now with the existence of high resolution JWST spectra (eg. S. Petrus et al. 2024).

The Community Aerosol and Radiation Model for Atmospheres, CARMA (R. P. Turco et al. 1979; O. B. Toon et al. 1988), is a bin-scheme microphysics model, and thus is able to resolve this problem and calculate cloud particle size distributions from first principles. CARMA is able to naturally reproduce a number of cloud features that other cloud models struggle to accurately model such as the brown dwarf and Hot Jupiter 10 μm silicate feature (D. Powell et al. 2019a), the day/night temperature contrast in Hot Jupiter atmospheres (P. Gao & D. Powell 2021), and the Hot Jupiter aerosol sequence (P. Gao et al. 2020). Beyond just these cases, CARMA is a well-tested and validated model that has been successfully applied to interpret detailed observations of clouds and aerosols both in our solar system—including sulfuric acid clouds on Venus (P. Gao et al. 2014), numerous studies of Earth’s clouds and aerosols (eg. Z. Chen et al. 2018; S. Lian et al. 2022; D. Rusch et al. 2017), CO₂ and water clouds on Mars (D. V. Michelangeli et al. 1993; A. Colaprete et al. 1999), clouds and hazes on Titan (E. L. Barth & O. B. Toon 2003, 2004, 2006), and hazes on Pluto (P. Gao et al. 2017)—and on extra-solar bodies such as Hot Jupiters (D. Powell et al. 2018; D. Powell & X. Zhang 2024), sub-Neptunes (P. Gao et al. 2023) and Y-dwarfs (J. Mang et al. 2022, 2024). CARMA is a flexible model, capable of simulating practically any condensate assuming enough is known about their physical properties.

Despite the strengths of CARMA as a model, it is only currently being used by a handful of researchers in the exoplanet community who have the required expertise to run the code. As a piece of legacy scientific software written in Fortran and developed over almost half a century, CARMA requires a large time investment to understand how the software works and how to run it. In light of this problem, we are releasing CARMapy—an open source python wrapper for CARMA which is designed to be user-friendly and well-documented in order to enable a wide range of researchers with minimal prior cloud modeling and/or Fortran expertise to effectively use it. CARMapy is based on the ExoCARMA (eg. D. Powell & X. Zhang 2024; P. Gao et al. 2020) version of CARMA 3.0 (C. G. Bardeen et al. 2008) and is well suited for modeling aerosol microphysics on exoplanets, as well as environments such as protoplanetary disks (D. Powell et al. 2019b). The upgrade to CARMapy, and the corresponding upgrade to the ExoCARMA base it runs on, has additionally provided greater flexibility on the types of condensates and atmospheres modelable while making the code significantly more efficient and implementing multithreading with OpenMP (L. Dagum & R. Menon 1998).

This paper will describe both CARMapy and the underlying ExoCARMA 2.0 version of CARMA. In Section 2.1 we will describe the history of CARMA and document the various changes made to the software over its nearly 50 year history, in the remainder of Section 2 we will describe the microphysical processes, along with our modeling assumptions and numerical methods, that are used in both CARMA and CARMapy, and in Section 3 we will demonstrate that CARMapy is able to replicate the results of previous versions of CARMA for a benchmark brown-dwarf case.

2. MODEL DESCRIPTION

2.1. Code Heritage

As CARMA has been continuously used over almost the past 50 years, multiple versions of CARMA have been developed. The original version of CARMA was written in Fortran 77 by R. P. Turco et al. (1979) and O. B. Toon et al. (1988). That model was then updated to CARMA 3.0 by C. G. Bardeen et al. (2008) who modernized the code to Fortran90. This main (Earth) CARMA branch is managed by the University Corporation for Atmospheric Research (UCAR) and is under active development today, being incorporated into the Community Earth System Model (CSEM, eg. S. Tilmes et al. 2023) and is actively being used to model cloud formation on Earth (eg. Z. Chen et al. 2018; S. Lian et al. 2022; D. Rusch et al. 2017). Additionally, branching in development history from the main CARMA branch are versions such as ExoCAM-CARMA (E. Wolf et al. 2022) which can model hazes in exoplanet atmospheres and PlanetCARMA (E. Barth 2020) which models clouds and hazes on solar system bodies. Our work, CARMapy, is built upon the ExoCARMA branch

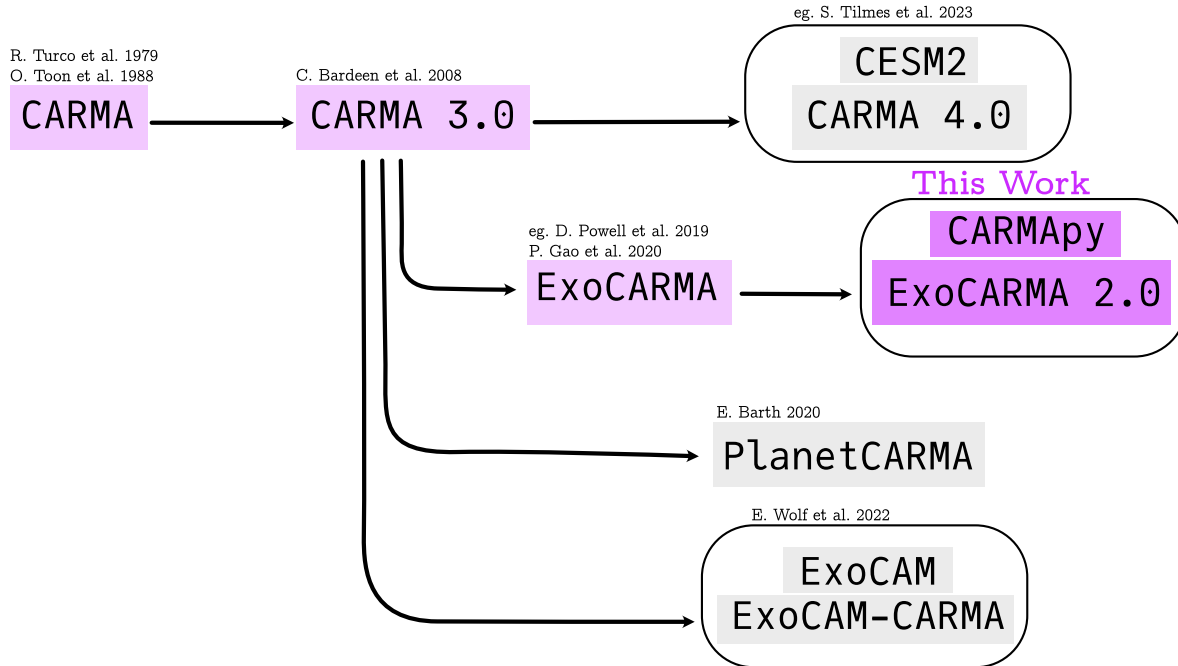


Figure 1. Diagram of the heritage of this work’s version of CARMA, along with selected other versions of CARMA

of CARMA. ExoCARMA branched from the development history of the main CARMA branch sometime in 2012, shortly after the release of CARMA 3.0. While the main Earth CARMA branch has been under active development since then, the majority of updates to that main branch since ExoCARMA branched from it have been to the sulfate chemistry so are unlikely to be relevant to the majority of exoplanets. We, however, intend to incorporate updates from the main Earth CARMA branch in the future.

This work presents two main codes—ExoCARMA 2.0 and CARMApy. ExoCARMA 2.0 is the most up to date version of ExoCARMA and includes a more flexible implementation for new condensates. CARMApy is a python wrapper built on top of this latest version of ExoCARMA, along with a suite of convenience functions which are useful for cloud microphysical modeling. CARMApy is designed in such a way that updates to ExoCARMA will propagate to CARMApy. A diagram showing the relationship of CARMApy to other versions of CARMA is shown in Figure 1

2.2. Cloud Microphysics

CARMA is a time-stepping, bin-scheme microphysical model. This means that cloud particles can form along a size distribution independently at each pressure level with the bin resolution on this grid controlled by the user. Upon initialization, the user specifies which microphysical processes to use among homogeneous and heterogeneous nucleation (see Sections 2.2.1, 2.2.2), condensational growth / evaporation (Section 2.2.3), and coagulation (Section 2.2.6). These processes are then simulated at each timestep, allowing particles to move from one bin to another. Particles are also transported between altitude bins following the vertical transport and settling schema described in Section 2.2.4.

2.2.1. Homogeneous Nucleation

CARMA models homogeneous nucleation—the first stage of cloud formation where particles form directly from the gas phase— following classical nucleation theory (H. Pruppacher & J. Klett 2010). Conceptually this process can be conceived of as arising out of the random motions of particles within an atmospheric cell. The random motions of gas particles will cause the microscopic density in every given location to fluctuate as gas particles temporarily stick to each other and then fly apart. Where these fluctuations cause a large enough clump of stuck-together gas particles to form, these (no-longer-gas) particles become bound to each other and thus nucleation occurs. Quantitatively, the production rate via homogeneous nucleation of particles per unit volume per unit time, J_{hom} is given by (P. Gao 2017, Eqn. A1)

$$J_{\text{hom}} = 4\pi a_c^2 \Phi Z n \exp(-\Delta F_c / kT) \quad (1)$$

where n is the number density of the vapor particles in the condensate's gas reservoir, k is the Boltzmann constant, and T is the temperature. The critical radius, a_c is defined as (H. Pruppacher & J. Klett 2010, Eqn. 7-27)

$$a_c = \frac{2M\sigma}{\rho_p RT \ln S} \quad (2)$$

where M , σ , ρ_p , and S are the molar mass, surface tension, density, and saturation ratio of the condensate and R is the ideal gas constant. The energy of formation, ΔF_c , of the condensate with radius a_c is given by (H. Pruppacher & J. Klett 2010, Eqns. 7-24, 7-26)

$$\Delta F_c = \max_a \left(4\pi a^2 \sigma - \frac{4\pi a^3}{3M} \rho_p RT \ln S \right) = \frac{4}{3} \pi \sigma a_c^2 \quad (3)$$

Fundamentally, the free energy of formation is a balance between the energy due to surface tension, which grows rapidly with radius a , and the decrease in free energy due to the volume of the particle growing larger. The first location where it is energetically favorable to continue growing the particle is the radius where the balance of these terms reaches its maximum, which occurs at $a = a_c$. Following a Boltzmann distribution, there should be $n \exp(-\Delta F_c/kT)$ particles at this unstable equilibrium where just one more molecule diffusing onto them will allow them rapidly grow. The rate at which a single molecule will diffuse onto these critically sized particles is given by $4\pi a_c^2 \Phi$ where Φ is the diffusion flux of the reservoir of gas molecules and is given by:

$$\Phi = n \sqrt{\frac{kT}{2\pi m_v}} \quad (4)$$

where m_v is the mass of an individual gas particle. Lastly, Z is the Zeldovich factor which accounts for non-equilibrium effects, such as the fact that particles at the critical radius can have a molecule evaporate from them instead of condense as well as the deviations from equilibrium caused by the fact that nucleation inherently introduces a max flux towards larger particles, is given by (H. Pruppacher & J. Klett 2010, Eqn. 7-44; Y. B. Zeldovich et al. 1992, Eqn. 16)

$$Z = \sqrt{\frac{\Delta F_c''}{-2\pi kT}} = \sqrt{\frac{\Delta F_c}{3\pi kT g_m^2}} \quad (5)$$

where $\Delta F_c''$ is the second derivative of the energy of formation, with respect to the number of molecule in the particle, at the critical radius, g_m is the number of molecules contained in a particle of radius a_c . Particles which nucleate homogeneously in CARMA are assigned to the particle bin closest to the critical radius, with the exact number of particles that nucleate being adjusted to conserve the total mass that nucleates.

2.2.2. Heterogeneous Nucleation

Heterogeneous nucleation occurs when a cloud particle condensates on top of an already existing particle of a different species, known as a cloud condensation nucleus (CCN) or more informally as a "seed particle." Similarly to homogeneous nucleation, heterogeneous nucleation occurs when the amount of the newly formed condensate adsorbed onto the CCN exceeds a critical amount and it becomes increasingly energetically favorable to adsorb new vapor molecules onto the heterogeneous particle. The heterogeneous nucleation rate, in units of new particles per unit time per CCN particle is (P. Gao 2017, Eqn. A.6)

$$J_{\text{het}} = 4\pi^2 r_N^2 a_c^2 \Phi_{\text{c surf}} Z_{\text{het}} \exp(-\Delta F_c f / kT), \quad (6)$$

where r_N is the radius of the CCN and a_c is the critical radius of the cluster of newly condensed particles that form on the surface of the CCN. Note that a_c is not the value of the radius of the heterogeneous particle after nucleation. The value of the critical radius, a_c , remains the same as in the homogeneous case as the local curved surface of the cluster must be in equilibrium with the vapor (once can also recover the same value for a_c by calculating out the volume of a spherical cap and maximizing the free energy as in Equation 3). The shape factor, f , accounts for the fact that the surface of the cluster of newly condensed particles is not exposed to air on all sides and is given by (H. Pruppacher & J. Klett 2010, Eqn. 9-27)

$$2f = 1 + \left(\frac{1 - \mu x}{\phi} \right)^4 + x^3 (2 - 4f_0 + f_0^3) + 3\mu x^2 (f_0 - 1) \quad (7)$$

where μ is the cosine of the contact angle between the condensate and the surface (with $\mu = 1$ being incredibly strongly interacting and $\mu = -1$ being non-interacting) and

$$x = r_N/a_c \quad (8)$$

$$\phi = \sqrt{1 - 2\mu x + x^2} \quad (9)$$

$$f_0 = (x - \mu)/\phi \quad (10)$$

We assume that the primary mechanism for particle growth is diffusion along the surface of the CCN so c_{surf} is the number density of condensate molecules on the surface of the CCN and is given by (P. Gao 2017, Eqn. A.11)

$$c_{\text{surf}} = \frac{\Phi}{\nu} \exp(F_{\text{des}}/kT) \quad (11)$$

Here, $\nu \exp(-F_{\text{des}}/kT)$ is the particle desorption rate, F_{des} is the desorption energy, and the pre-exponential factor, ν , can be interpreted as the attempt frequency for particle escape. We estimate ν using the energy of a harmonic oscillator ($E = 1/2m\omega^2 A^2$) following the methods of A. G. G. M. Tielens & L. J. Allamandola (1987, Eqn. 6)⁴

$$\nu = \sqrt{\frac{2N_s F_{\text{des}}}{\pi^2 m_v}} \approx (1.6 \times 10^{11} \text{s}^{-1}) \left(\frac{F_{\text{des}}/k}{1\text{K}}\right)^{1/2} M_v^{-1/2} \quad (12)$$

where M_v is the molar mass of the vapor particle and N_s is the density of adsorption sites on the CCN and is identified with the reciprocal square amplitude of adsorbant oscillation. N_s is frequently approximated as $N_s \approx 1.5 \times 10^{15} \text{cm}^{-2}$, which corresponds to an average distance between sites of $\sim 3\text{\AA}$. CARMApy defaults to assuming that the desorption energy is equal to half the latent heat of evaporation of a single molecule

Lastly, the heterogeneous Zeldovich factor is given by (H. Vehkamäki et al. 2007, Eqn. 17):

$$Z_{\text{het}} = Z \sqrt{\frac{4\phi^3}{2\phi^3 + (1 - \mu x)(2 - 4\mu x - (\mu^2 - 3)x^2)}} \quad (13)$$

Similar to homogeneous nucleation, the $4\pi r_N^2 c_{\text{surf}} \exp(-\Delta F_c f/kT)$ Boltzman factor in the definition of J_{het} can be interpreted as the number of sites on each CCN which are at the critical radius, a_c , and thus will continue to grow if they adsorb another particle. Likewise the $\pi a_c^2 \Phi$ factor is the rate at which particles will reach these critical sites (note that we use a surface area of πa_c^2 instead of $4\pi a_c^2$ like we did for homogeneous nucleation because in the case of heterogeneous nucleation, the cluster of particles is touching the CCN and thus not all of the surface area is available for the adsorption of additional particles). Note that the units of J_{het} are in new particles per unit time per CCN, so to get the heterogeneous nucleation rate in the same units as J_{hom} we must multiply by the number density of the CCN. In CARMA, it is assumed that heterogeneous nucleation does not significantly alter the mass of the particle—as the bin sizes in CARMA grow exponentially larger with each successive bin, this assumption hold for most cases.

2.2.3. Condensational Growth/Evaporation

Condensation and evaporation (or more specifically, but equivalently mathematically, solid deposition and sublimation as most of our particles are solids) occur when a vapor molecule diffuses onto or away from the surface of a cloud particle. If we assume that particles are large compared to the mean free path of the vapor ($Kn \gg 1$, we will relax this assumption later), we can invoke Fick's first law of diffusion and so the rate of change in mass, m , of a cloud particle can be described as (M. Z. Jacobson 2005, Eqn. 16.1)

$$\frac{dm}{dt} = 4\pi R_d^2 D_v \frac{d\rho_v}{dR_d} \quad (14)$$

where R_d is the radial distance from the center of the particle, $d\rho_v/dR_d$ is the radial gradient of vapor density and D_v is the molecular diffusion coefficient of the vapor, which is given by (M. Z. Jacobson 2005, Eqn. 16.17)

$$D_v = \frac{5}{16N_A d_q^2 \rho_a} \sqrt{\frac{RTM_a}{2\pi} \left(\frac{M + M_a}{M}\right)} \quad (15)$$

⁴ We note that this method is often cited as T. I. Hasegawa et al. (1992) even though the authors of that work themselves cite A. G. G. M. Tielens & L. J. Allamandola (1987) for this equation

where M_a is the molar mass of the atmosphere, N_A is Avogadro's number, ρ_a is the local density of the atmosphere, and d_q is the collision diameter of the gas molecule.

We assume that near the surface of the drop the vapor density is set by the saturation vapor pressure (along with the ideal gas law) so $\rho_v(R_d = r) = \rho_s$. If we now integrate Equation 14 from $R_d = r$ at the particles surface to $R_d = \infty$ we find that the growth/evaporation rate is given by (M. Z. Jacobson 2005, Eqn. 16.2)

$$\frac{dm}{dt} = 4\pi r D_v (\rho_v - \rho_s) \quad (16)$$

As we expect, when the atmosphere is supersaturated ($\rho_v > \rho_s$) the particles will grow and when the atmosphere is not saturated ($\rho_v < \rho_s$) the particle will evaporate. Due to the latent heat of evaporation, however, these processes will change the temperature of the particle, thus changing their saturation vapor pressure. To account for this, the heating due to condensation and evaporation is given by (M. Z. Jacobson 2005, Eqn. 16.5)

$$m c_p \frac{dT_p}{dt} = L \frac{dm}{dt} - \frac{dQ}{dt} \quad (17)$$

where c_p is the specific heat capacity of the particle, L is the latent heat of evaporation of the condensate, and T_p is the temperature of the particle. This heat is conducted away from the particle following (M. Z. Jacobson 2005, Eqn. 16.3)

$$\frac{dQ}{dt} = -4\pi R_d^2 \kappa_a \frac{dT}{dR_d} \quad (18)$$

where κ_a is the heat capacity of the atmosphere. Combining Equations 14, 17, and 18, along with the ideal gas law and the Clausius-Clapeyron equation ($d \ln p_s / dT = L / RT^2$), and assuming the temperature of the particle is in steady state and $LM/RT - 1 \approx LM/RT$, our new equation for condensational growth / evaporation is (P. Gao 2017, A.15)

$$\frac{dm}{dt} = \frac{4\pi r D_v p_s (S - 1)}{\frac{RT}{M} + \frac{D_v L^2 M p_s}{\kappa_a T^2}} \quad (19)$$

where p_s is the saturation vapor pressure.

We consider three further corrections to this equation. Firstly, this equation was derived assuming we can treat the vapor as a continuum—this breaks down at small particle sizes where the mean free path of the vapor becomes comparable in value to the size of the particles. To correct for this assumption we introduce a corrected diffusion coefficient and thermal conductivity (M. Z. Jacobson 2005, Eqns. 16.19, 16.27)

$$D'_v = \frac{D_v}{1 + \lambda_c \text{Kn}_c} \quad (20)$$

$$\kappa'_a = \frac{\kappa_a}{1 + \lambda_t \text{Kn}_t} \quad (21)$$

where λ_c and λ_t are coefficients given by

$$\lambda_c = \frac{1.33 \text{Kn}_c + 0.71}{\text{Kn}_c + 1} \quad (22)$$

$$\lambda_t = \frac{1.33 \text{Kn}_t + 0.71}{\text{Kn}_t + 1} \quad (23)$$

and Kn_c and Kn_t are the collisional and energy exchange Knudsen numbers of the condensing gas with respect to the particle and are defined as (M. Z. Jacobson 2005, Eqns. 16.28, 16.29)

$$\text{Kn}_c = \frac{\ell_c}{r} = \frac{3D_v}{r} \sqrt{\frac{\pi M}{8RT}} \quad (24)$$

$$\text{Kn}_t = \frac{\ell_t}{r} = \frac{3\kappa_a}{r\rho_a \left(c_p - \frac{R}{2M_a}\right)} \sqrt{\frac{\pi M}{8RT}} \quad (25)$$

where the ℓ_i s are the mean free paths. Low Knudsen numbers indicate that the particle frequently interacts with vapor molecules and thus the continuum assumption is valid, while large Knudsen numbers imply the continuum assumption fails.

Secondly, the vapor pressure over a curved surface is different than that over a flat surface—an phenomenon known as the Kelvin effect. To correct for this effect we introduce the Kelvin factor (M. Z. Jacobson 2005, Eqns. 16.33)

$$A_k = \frac{p_{s,\text{curved}}}{p_{s,\text{flat}}} = \exp\left(\frac{2M\sigma}{\rho_p RT r}\right) \quad (26)$$

Lastly, particles which are moving generate eddies which sweep additional energy and mass onto the particle. To account for this, we introduce two ventilation factors, F_v and F_t , which were determined empirically from water droplets (H. Pruppacher & J. Klett 2010, Eqns. 13-60, 13-61)

$$F_v = \begin{cases} 1 + 0.108x_v^2 & x_v \leq 1.4 \\ 0.78 + 0.308x_v & x_v > 1.4 \end{cases} \quad x_v = Re^{1/2} \left(\frac{\eta_a}{\rho_a D'_v}\right)^{1/3} \quad (27)$$

$$F_t = \begin{cases} 1 + 0.108x_t^2 & x_t \leq 1.4 \\ 0.78 + 0.308x_t & x_t > 1.4 \end{cases} \quad x_t = Re^{1/2} \left(\frac{\eta_a c_p}{\kappa'_a}\right)^{1/3} \quad (28)$$

where η_a is the kinematic viscosity of the air and Re is the Reynolds number (see Section 2.2.4). After applying all of these corrections, the formula for condensational growth / evaporation used in CARMA is (P. Gao 2017, Eqn. A.16)

$$\frac{dm}{dt} = \frac{4\pi r D'_v p_s (S - A_k)}{\frac{RT}{MF_v} + \frac{D'_v M L^2 p_s}{\kappa'_a RT^2 F_t}} \quad (29)$$

Just as with vertical transport below, CARMA uses the piecewise parabolic method (P. Colella & P. R. Woodward 1984) to “transport” particles between mass bins.

2.2.4. Particle Sedimentation

The problem of particle sedimentation can be split into three regimes—laminar ($Re < 1$), transitional ($1 < Re < 1000$), and turbulent ($Re > 1000$). Both the laminar and turbulent regimes have simple formulae for the sedimentation (terminal) velocities but there is no simple closed form equation for the transitional regime. Additionally, it is required to know the velocity of particles in order to determine which fall velocity regime to use, creating a circular problem.

To resolve these issues, we begin by assuming that the particles are in the laminar regime (i.e. they are small and slow moving) and thus their sedimentation velocity, v_t , can be described by Stokes’ fall velocity

$$v_t = \frac{2}{9} \frac{g r^2 C_c (\rho_p - \rho_a)}{\eta_a} - v_{\text{winds}} \quad (30)$$

where g is the gravitational acceleration, v_{winds} is a user defined upward wind speed, and C_c is the Cunningham slip factor which is given by (N. A. Fuchs 1964, Eqn. 8.5)

$$C_c = 1 + \text{Kn} \left(1.256 + 0.42e^{-0.87/\text{Kn}}\right) \quad (31)$$

where the numerical constants in this equation are empirically derived from falling oil drops and Kn is a Knudsen number given by:

$$\text{Kn} = \frac{\ell}{r} = \frac{2\eta_a}{\rho_a} \sqrt{\frac{\pi M_a}{8RT}} \quad (32)$$

The Reynolds number is defined as follows

$$Re = \frac{2r\rho_a(v_t + v_{\text{winds}})}{\eta_a} \quad (33)$$

If $Re < 1$ then our assumption that particles are small and slow moving is valid and we use Equations 30 and 33 for v_t and Re respectively. Otherwise, we must instead calculate the fall velocity in the transition ($1 < Re < 1000$) or

Coefficient	Value
B_0	-3.18657
B_1	+0.992696
B_2	-1.53193×10^{-3}
B_3	-9.87059×10^{-4}
B_4	-5.78878×10^{-4}
B_5	$+8.55176 \times 10^{-5}$
B_6	-3.27815×10^{-6}

Table 1. Empirical coefficients for the fit given in Equation 36 (H. Pruppacher & J. Klett 2010).

Newtonian ($Re > 1000$) regimes. For these regimes we introduce the drag coefficient, C_D , which is defined such that the terminal velocity is as (J. H. Seinfeld & S. N. Pandis 1998, Eqn. 8.44)

$$v_t = \left(\frac{8gr(\rho_p - \rho_a)}{3C_D\rho_a} \right)^{1/2} - v_{\text{winds}} \quad (34)$$

Combining this with equation 33 we can define a quantity, $C_D Re^2$, sometimes known as the Best number, as follows (H. Pruppacher & J. Klett 2010, Eqn. 10-142)

$$C_D Re^2 = \frac{32r^3\rho_a(\rho_p - \rho_a)g}{3\eta_a^2} \quad (35)$$

We can now use this value to find the Reynolds number using the following empirical fit (H. Pruppacher & J. Klett 2010, Eqn. 10-145):

$$\ln Re = B_0 + B_1x + B_2x^2 + \dots + B_6x^6 \quad (36)$$

where $x = \ln(C_D Re^2)$ and the B_i are given in Table 1. If $Re < 1000$ we then calculate the fall velocity from Equation 33 as follows

$$v_t = \frac{\eta_a Re}{2\rho_a r} - v_{\text{winds}} \quad (37)$$

If instead $Re > 1000$, we set $C_D = 0.45$ and calculate the fall velocity from Equation 34.

2.2.5. Eddy Diffusion

In addition to particle sedimentation, CARMA also tracks particle diffusion, allowing for the vertical lofting of cloud particles. We assume that eddy (turbulent) diffusion dominates molecular diffusion, as is expected to be true in all but the very upper atmosphere P. Woitke et al. (2020), and thus the diffusive velocities are given by

$$v_{ed} = -K_{zz} \frac{d \ln f_r}{dz} \quad (38)$$

where f_r is the particle mixing ratio and where K_{zz} is the eddy diffusion coefficient.

As in for particle advection in mass space, particles are transported between altitude bins using the piecewise parabolic method.

2.2.6. Coagulation/Coalescence

When two condensate molecules collide with each other, depending on their mass and momenta, there are largely three classes of outcomes—they can stick together, they can bounce off each other, or they can fragment into pieces (C. Güttler et al. 2010). To model these collisional processes, we thus must model both the rate at which particles collide and then the outcomes of that collision. CARMA considers three sources for collisions—Brownian motion, convective diffusion enhancement, and gravitational coalescence (also known as differential settling). Brownian motion and gravitational coalescence are common processes considered other microphysical cloud models (K. Ohno & S. Okuzumi 2017; E. K. H. Lee & K. Ohno 2025b), whereas convective diffusion enhancement serves as a correction term for the Brownian motion term. We note that while others have found that large scale atmospheric turbulence can be an important source of collisions near the cloud base (D. Samra et al. 2022), CARMA does not currently consider turbulence

as a collision source. CARMA assumes that Brownian motion (and thus convective diffusion enhancement) causes particles which collide to stick together and form compact, spherical (ie non-fractal) particles with 100% probability while CARMA allows particles that collide due to differential settling to either bounce or stick according to a formulism discussed below. CARMA does not consider fragmentation as an outcome of collisions.

The Brownian coagulation kernel, for coagulation between two particles, 1 and 2, K_{12}^b , which represents the collision probability of two particles undergoing thermal motion is given by (N. A. Fuchs 1964, Eqns. 49.26, M. Z. Jacobson 2005, Eqns. 15.33)

$$K_{12}^B = K_{21}^B = 4\pi(D_1 + D_2)(r_1 + r_2)\beta \quad (39)$$

Where the D_i and r_i are the molecular diffusion coefficients and radii of the populations of particles and β is a interpolation factor that interpolates between the continuum and kinetic regimes. The molecular diffusion coefficients are given by (M. Z. Jacobson 2005, Eqn. 15.29)

$$D_i = \frac{kTC_c}{6\pi\eta_\alpha r_i} \quad (40)$$

where C_c is the Cunningham slip factor (see Equation 31). The interpolation factor, β , is given by (N. A. Fuchs 1964, Eqn. 49.27)

$$\frac{1}{\beta} = \frac{r_1 + r_2}{r_1 + r_2 + \sqrt{\delta_1^2 + \delta_2^2}} + \frac{4(D_1 + D_2)}{(r_1 + r_2)\sqrt{v_1^2 + v_2^2}} \quad (41)$$

where the v_i are the thermal velocities of the particles and are given by

$$v_i = \sqrt{\frac{8kT}{\pi m_i}} \quad (42)$$

where m_i is the mass of the particles. The transition length scale, δ_i , is given by (M. Z. Jacobson 2005, Eqn 15.34)

$$\delta_i = \frac{(2r_i + \ell_i)^3 - (4r_i^2 + \ell_i^2)^{3/2}}{6r_i\ell_i} - 2r_i \quad (43)$$

with ℓ_i being the mean free path of the particle given by

$$\ell_i = \frac{8D_i}{\pi v_i} \quad (44)$$

In a similar mechanism to the ventilation coefficients discussed in Section 2.2.3, falling large particles generate eddies which can draw smaller particles onto them. This convective diffusion enhancement increases the coagulation rate of large particles and its kernel, K^{DE} , is given by (M. Z. Jacobson 2005, Eqn. 15.35)

$$K_{12}^{DE} = \begin{cases} \alpha_{lo} K_{12}^B Re_j^{1/3} \left(\frac{\eta}{\rho D_i}\right)^{1/3} & Re_j \leq 1 \\ \alpha_{hi} K_{12}^B Re_j^{1/2} \left(\frac{\eta}{\rho D_i}\right)^{1/3} & Re_j \geq 1 \end{cases}, \quad (r_j \geq r_i) \quad (45)$$

where we take $\alpha_{lo} = \alpha_{hi} = 0.45$.⁵

Lastly, we consider the effects of gravitational coalescence. As particles fall with differing fall velocities they can collide and then coalesce together. The kernel for this process is given by

$$K_{12}^G = E_{\text{collide}} E_{\text{coalesce}} \pi (r_1 + r_2)^2 |v_{t,1} - v_{t,2}| \quad (46)$$

where E_{collide} and E_{coalesce} are the collision and coalescence efficiencies respectively and $v_{t,1}$ and $v_{t,2}$ are the terminal fall velocities of the two particles.

We set $E_{\text{collide}} = \max(E_{\text{Langmuir}}, E_{\text{Fuchs}})$ where E_{Langmuir} is given by (I. Langmuir 1948, Eqn. 23)

$$E_{\text{Langmuir}} = \frac{E_V + E_A Re_j / 60}{1 + Re_j / 60} \quad (r_j \geq r_i) \quad (47)$$

⁵ See Chapter 17 of H. Pruppacher & J. Klett (2010) for discussion of this value.

where E_V and E_A are the efficiencies in the viscous ($Re_j \ll 1$) and aerodynamic ($Re_j \gg 1$) cases respectively and are given by (I. Langmuir 1948, Eqns. 16, 23)

$$E_V = \begin{cases} \left(1 + \frac{0.75 \ln 2S_k}{S_k - 1.214}\right)^{-2} & S_k > 1.214 \\ 0 & S_k \leq 1.214 \end{cases} \quad (48)$$

$$E_A = \begin{cases} \frac{S_k^2}{(S_k + 1/2)^2} & S_k \geq 1/12 \\ 0 & S_k < 1/12 \end{cases} \quad (49)$$

where S_k is the Stokes number and is given by

$$S_k = \frac{v_{t,i} |v_{t,j} - v_{t,i}|}{r_j g}, \quad (r_j \geq r_i) \quad (50)$$

The E_{Fuchs} term in our definition of E_{collide} is the collision efficiency given by (N. Fuchs 1951; S. K. Friedlander 1957; H. Pruppacher & J. Klett 2010, Eqn. 11-86), designed to correct E_{Langmuir} for the direct interception caused by non-point fine particles (see N. A. Fuchs 1964, §54)

$$E_{\text{Fuchs}} = \frac{(r_j/r_i)^2}{2(1 + (r_j/r_i))^2}, \quad r_j > r_i \quad (51)$$

Finally, E_{coalesce} , which captures the effect that particles may collide and then ‘bounce-off,’ is empirically determined for raindrops and is given by (K. V. Beard & H. T. Ochs III 1984, Eqn. 4):

$$E'_{\text{coalesce}} = (a - b)^{1/3} - (a + b)^{1/3} + 0.459 \quad (52)$$

where

$$a = \sqrt{b^2 + 0.00441} \quad (53)$$

$$b = 0.946\beta - 0.319 \quad (54)$$

$$\beta = \ln\left(\frac{r_i}{1 \mu\text{m}}\right) + 0.44 \ln\left(\frac{r_j}{200 \mu\text{m}}\right), \quad (r_j > r_i) \quad (55)$$

where we bound E_{coalesce} to be between 0.5 and 1.0; that is

$$E_{\text{coalesce}} = \max(0.5, \min(1.0, E'_{\text{coalesce}})) \quad (56)$$

The total coagulation kernel is now given by:

$$K_{12}^{\text{tot}} = K_{12}^B + K_{12}^{DE} + K_{12}^G \quad (57)$$

2.2.7. A Note on Supersaturation Ratios

The standard supersaturation ratio of a vapor, S , is defined as the ratio of the partial pressure of the vapor p_v to the saturation vapor pressure, p_s . That is:

$$S = \frac{p_v}{p_s} \quad (58)$$

For Type III reactions (C. Helling & P. Woitke 2006, Appendix B), however, which involve more than one molecular product or more than one molecular reactant, grain chemistry models show that the effective supersaturation ratio for the reaction can instead be expressed as

$$S_r = S^{1/\nu_r^{\text{key}}} \quad (59)$$

where, ν_r^{key} , is the stoichiometric ratio of the limiting reactant in the reaction. For the above microphysical equations, this effective supersaturation ratio, S_r , is used in place of the standard supersaturation ratio for type III reactions.

2.3. Numerical Methods

Given the number density vector of all gas and particle bins at timestep t , \mathbf{n}^t , the number density vector at the next time step can be determined by simultaneous application of operators, $\mathcal{L}_{\text{proc}}$, representing the effects of the various modeled processes:

$$\mathbf{n}^{t+1} = (\mathcal{L}_{\text{transport}} + \mathcal{L}_{\text{coagulation}} + \mathcal{L}_{\text{growth/evap}} + \mathcal{L}_{\text{nuc}} + \mathcal{L}_{\text{gas depletion}})\mathbf{n}^t \quad (60)$$

CARMA implements an operator splitting method where in each timestep vertical transport is first calculated; then coagulation; then nucleation, growth, and evaporation; and then finally gas depletion. Put formally in our operator notation that is

$$\mathbf{n}^{t+1} = \mathcal{L}_{\text{gas depletion}}(\mathcal{L}_{\text{growth/evap}} + \mathcal{L}_{\text{nuc}})\mathcal{L}_{\text{coag}}\mathcal{L}_{\text{transport}}\mathbf{n}^t \quad (61)$$

The following subsections describe how CARMA implements these various operators.

2.3.1. Particle Transport

Cloud particles and gas are advected between bins (both altitude level bins, and for clouds, particle mass bins) using the piecewise parabolic method (PPM). A full description of this method is presented in Section 1 of [P. Colella & P. R. Woodward \(1984\)](#)—we only outline the broad steps of the method. The PPM is used to solve the linear advection equation

$$\frac{\partial n}{\partial t} + u \frac{\partial n}{\partial \xi} = 0 \quad (62)$$

where n is the particle concentration, ξ is a generalized coordinate (eg. altitude or mass), and u is a generalized advection velocity. If we let n_k be the particle concentration in bin k and let $\xi_{k-1/2}$ and $\xi_{k+1/2}$ be the boundaries of that bin, the relationship between the continuous particle distribution at timestep t , $n(\xi, t)$, and the binned particle concentration at the same timestep is simply the averaged concentration across the bin:

$$n_k^t = \frac{1}{\xi_{k+1/2} - \xi_{k-1/2}} \int_{\xi_{k-1/2}}^{\xi_{k+1/2}} n(\xi, t) d\xi \quad (63)$$

Similarly, we can update this distribution by solving Equation 62 as follows:

$$n_k^{t+1} = \frac{1}{\xi_{k+1/2} - \xi_{k-1/2}} \int_{\xi_{k-1/2}}^{\xi_{k+1/2}} n(\xi - u\Delta t, t) d\xi \quad (64)$$

The problem with this method, however, is we do not know the continuous distribution $n(\xi, t)$, we only know the discrete distribution n_k^t . The PPM scheme solves this problem by introducing parabolic interpolation functions in each bin. These parabolas are chosen such that existing local extrema are preserved and no local extrema are introduced. These conditions require that the parabolae are monotonic within each bin, and constant at the local minima and maxima of the discrete distribution.

We seek a form for the advective flux across each boundary which splits into the upwards and downwards flux where each term only depends on the number density in one bin (dropping the t for clarity):

$$F_{\text{ad}, k+1/2} = n_k v_{\text{ad}, k+1/2}^{\uparrow} - n_{k+1} v_{\text{ad}, k+1/2}^{\downarrow} \quad (65)$$

If at the $k + 1/2$ boundary $u > 0$, then $v_{\text{ad}, k+1/2}^{\downarrow} = 0$ and

$$n_{k+1/2} v_{\text{ad}, k-1/2}^{\uparrow} = F_{\text{ad}, k+1/2} = -\frac{1}{\Delta\xi\Delta t} \int_{\xi_{k+1/2}-u_{k+1/2}\Delta t}^{\xi_{k+1/2}} n(\xi) d\xi \quad (66)$$

where $\Delta\xi = \xi_{k+1/2} - \xi_{k-1/2}$ is the width of the bin. Similarly, if $u < 0$ then $v_{\text{ad}, k+1/2}^{\uparrow} = 0$

$$n_{k+1/2} v_{\text{ad}, k-1/2}^{\downarrow} = F_{\text{ad}, k-1/2} = -\frac{1}{\Delta\xi\Delta t} \int_{\xi_{k-1/2}}^{\xi_{k-1/2}-u_{k-1/2}\Delta t} n(\xi) d\xi \quad (67)$$

2.3.2. Eddy Diffusion

The net flux due to diffusion, F_{dif} , can be described as

$$F_{\text{dif}} = nv_{\text{ed}} = -nK_{zz} \frac{d \ln f_r}{dz} = -\rho_a K_{zz} \frac{df_r}{dz} \quad (68)$$

We similarly seek an expression for the flux across the bin boundaries of the form

$$F_{\text{dif}, k+1/2} = n_k v_{\text{dif}, k+1/2}^{\uparrow} - n_{k+1} v_{\text{dif}, k+1/2}^{\downarrow} \quad (69)$$

Assuming that between bins the atmospheric pressure profile follows an exponential profile, the effective velocity coefficients can be written as

$$v_{\text{dif}, k+1/2}^{\uparrow} = \frac{K_{zz} \ln(\rho_k / \rho_{k+1})}{\Delta z \frac{\rho_k}{\rho_{k+1}} - 1} \quad (70)$$

$$v_{\text{dif}, k+1/2}^{\downarrow} = \frac{\rho_k}{\rho_{k+1}} v_{\text{dif}, k+1/2}^{\uparrow} \quad (71)$$

Now having the effective velocities for each of these processes at each boundary between bins, CARMA solves the following mass conservation equation

$$\frac{\partial n}{\partial t} + \nabla \cdot (F_{\text{dif}} + F_{\text{ad}}) = 0 \quad (72)$$

For a given layer we can write this equation as

$$n_k^{t+1} - n_k^t = \frac{\Delta t}{\Delta z} \left(v_{k-1/2}^{\uparrow} n_{k-1}^* + v_{k+1/2}^{\downarrow} n_{k+1}^* - \left(v_{k-1/2}^{\downarrow} + v_{k+1/2}^{\uparrow} \right) n_k^* \right) \quad (73)$$

where $v_{k+1/2}^{\uparrow} = v_{\text{ad}, k+1/2}^{\uparrow} + v_{\text{dif}, k+1/2}^{\uparrow}$ and so on. We use the notation n^* on the right hand side in this equation as CARMA can either solve this equation explicitly, using n^t in place of n^* , or implicitly, using n^{t+1} instead. For efficiency purposes, if the entire column is stable under the explicit scheme ($\frac{\Delta z_k}{\Delta t} > v_{k-1/2}^{\downarrow} + v_{k+1/2}^{\uparrow}$ for all k), the explicit scheme is used for the column. Otherwise CARMA switches to the implicit scheme and uses the Thomas tridiagonal Algorithm (D. R. Durran 1999, §A.2) as the transport equation describes a tridiagonal matrix which is diagonally dominant, so the algorithm is guaranteed to be stable.

2.3.3. Coagulation

Following M. Z. Jacobson et al. (1994), the changes in particle abundance due to coagulation is calculated using a semi-implicit method. The equation which we solve is

$$\frac{dn}{dt} = S - Ln \quad (74)$$

where S is the source (production) term and L is the loss rate. Put in semi-implicit finite difference form, this is

$$\frac{n_k^{t+1} - n_k^t}{\Delta t} = S_k - L_k n_k^{t+1} \quad (75)$$

with S and L calculated at the start of the timestep. This means that the updated number density is thus

$$n_k^{t+1} = \frac{n_k^t + S_k \Delta t}{1 + L_k \Delta t} \quad (76)$$

This implicit form guarantees that particle concentration never becomes negative.

The loss term, assuming the resulting product completely leaves bin k , for example by colliding with a different species, is

$$L_k = \sum_j K_{jk} n_j^t \quad (77)$$

Under the same assumption, the source term can be written as⁶

$$S_k = \sum_{k < i+j < k+1} K_{ij} n_i^{t+1} n_j^t P_{ijk}^\downarrow + \sum_{k-1 < i+j < k} K_{ij} n_i^{t+1} n_j^t P_{ijk-1}^\uparrow \quad (78)$$

where P_{ijk}^\downarrow and P_{ijk}^\uparrow are partition factors to account for the fact that the mass of created particle likely falls between bins. Since the sum treats the orderings (i, j) and (j, i) as separate terms, P_{ijk}^\downarrow and P_{ijk}^\uparrow can be straightforwardly derived from the conservation of the source particle's mass ($P_{ijk}^\downarrow m_k + P_{ijk}^\uparrow m_{k+1} = m_i$) and normalization to the mass fraction ($P_{ijk}^\downarrow + P_{ijk}^\uparrow = m_i/m_{i+j}$):

$$P_{ijk}^\downarrow = \frac{m_i}{m_{i+j}} \frac{r_m m_k - m_{i+j}}{(r_m - 1)m_k} \quad (79)$$

$$P_{ijk}^\uparrow = \frac{m_i}{m_{i+j}} \frac{m_{i+j} - m_k}{(r_m - 1)m_k} \quad (80)$$

where $r_m = m_{k+1}/m_k$ is the mass ratio between bins and $m_{i+j} = m_i + m_j$ (the P_{ijk} are bounded between 0 and 1). Note that $P_{ijk}^\uparrow + P_{jik}^\uparrow + P_{ijk}^\downarrow + P_{jik}^\downarrow = 1$ which is the expected number conservation. Also note that in our calculation of S_k we consider the number density of the source (n_i^{t+1}) and partner (n_j^t) species at different time steps. This is because if we were to make this term fully implicit with the partner species being evaluated also at $t+1$ we would break mass conservation—the loss term is calculated semi-implicitly so the production term also needs to be calculated semi-implicitly.

In cases of self collision where part of the resulting particle lies still within the source bin ($m_i < m_{i+j} < m_{i+1}$), which might happen if a particle collides with a particle in the same bin or with a smaller particle of the same species, we consider the part of the source particle that remains to contribute neither to the production nor the loss. This means that we set $P_{ijk}^\downarrow = 0$ if $i = k$ (note that the P_{ijk}^\uparrow remains as is as it is used for the updating bin $i+1$, not bin i). We similarly adjust the loss term to account for the fact that we do not treat the P_{ijk}^\downarrow as part of the production term when $i = k$:

$$L_k = \sum_{j+k \not< k+1} K_{kj} n_j^t + \sum_{j+k < k+1} K_{kj} n_j^t (1 - P_{kjk}^\downarrow) \quad (81)$$

2.3.4. Growth, Evaporation, and Nucleation

Similar to coagulation, growth, evaporation, and nucleation are simultaneously calculated using a semi-implicit method as follows

$$n_k^{t+1} = \frac{n_k^t + S_k \Delta t}{1 + L_k \Delta t} \quad (82)$$

The source term for these processes can be written as

$$S_k = J_{\text{hom}} + \sum_i J_{ki} n_i^t + v_{\text{grow}, k-1/2}^\uparrow n_{k-1}^t + v_{\text{evap}, k+1/2}^\downarrow n_{k+1}^t + S_{\text{het evap}} \quad (83)$$

where $\sum_i J_{ki} n_i^t$ describes all the heterogeneous nucleation events which produce particles in bin k where particles in bin i served as CCN, $v_{\text{grow}, k-1/2}^\uparrow$ and $v_{\text{evap}, k+1/2}^\downarrow$ are analogous to $v_{\text{ad}, k-1/2}^\uparrow$ and $v_{\text{ad}, k+1/2}^\downarrow$ and describe the growth rate from the bin below and evaporation rate from the bin above respectively, and $S_{\text{het evap}}$ describes the cores left behind by evaporating heterogeneous species.

The loss term can be written as

$$L_k = \sum_i J_{ik} + v_{\text{grow}, k+1/2}^\uparrow + v_{\text{evap}, k-1/2}^\downarrow \quad (84)$$

where $\sum_i J_{ik}$ describes the nucleation events where the current bin, bin k , serves as the CCN.

⁶ To clarify the notation: $i < j$ if and only if $m_i < m_j$ and i and j are of the same condensate species, even if different sizes

2.3.5. Gas Depletion

After the rest of the processes are considered, **CARMA** depletes the gas phase in an explicit forward Euler scheme conserving mass from timestep to timestep. That is **CARMA** calculates the amount of new condensate created or destroyed in each layer by nucleation, growth, and evaporation and then adjusts the gas phase to balance those processes. Numerically this means that

$$n_{\text{gas}}^{t+1} - n_{\text{gas}}^t = \sum_{\text{cloud}} (n_{\text{cloud}}^{t+1} - n_{\text{cloud}}^t) \frac{m_{\text{cloud}}}{m_{\text{gas}}} \frac{\nu_{\text{cloud}}^{\text{gas}} M_{\text{gas}}}{M_{\text{cloud}}} \quad (85)$$

where the sum is over every bin of every cloud species and $\nu_{\text{cloud}}^{\text{gas}}$ is the stoichiometric ratio of the reaction that forms the condensate species for the gas in question. As the gas depletion scheme in **CARMA** is explicit it can cause the gas abundance to become negative. If this is the case, **CARMA** substeps at half the timestep, restarting the growth, evaporation, and nucleation calculations.

2.3.6. A Note on Heterogeneous Particles

If a particle is heterogeneous, meaning it formed by heterogeneous nucleation or coagulation between two particles of different compositions, **CARMA** treats this particle as a shell material which is exposed to the gas phase and a core material which is isolated from the gas phase. This means that when these particles grow or evaporate, they use only the shell material as the material properties for these processes. Additionally, as these particles grow, evaporate, coagulate, and move around in the atmosphere, **CARMA** tracks the total amount of mass that is trapped in the core in each size and altitude bin. If at any point, the average mass in the core exceeds the mass of the bin, the particles are considered to have evaporated their shell material. The core material is then deposited into the pure material's bins into the two bins closest to the heterogeneous species mass bin, conserving both mass and number. This process uses partition functions analogous to those used in coagulation and determines the $S_{\text{het evap}}$ term in Eqn. 83.

2.4. Atmospheric Characteristics

Some of the above microphysical processes depend on either the thermal conductivity of the atmosphere, the viscosity of the atmosphere, and/or the specific heat capacity of the atmosphere. **CARMApy** requires a constant heat capacity but allows for the thermal conductivity and viscosity to change as a function of temperature. The thermal conductivity of the atmosphere, κ_a is parameterized as follows:

$$\kappa_a = \kappa_0 + \kappa_1 T + \kappa_2 T^2 \quad (86)$$

with the κ_i being user specified parameters. The dynamic viscosity of the atmosphere, $\mu_a = \rho_a \eta_a$, is parameterized as follows

$$\mu_a = \frac{\mu_1 (T/1 \text{ K})^{\mu_2}}{1 + \mu_3/T + \mu_4 T^2} \quad (87)$$

where the μ_i are parameters fit to empirical data.

CARMApy includes a default parameter set assuming a pure H_2 atmosphere, which is a reasonable assumption for bodies such as hot Jupiters and brown dwarfs, and allows users to set the atmospheric parameters to user defined values. The **CARMApy** default atmospheric parameters are presented in Table 2. We point the reader to [E. W. Lemmon \(2025\)](#) for thermal conductivity values and to Table 2-138 of [D. W. Green & M. Z. Southard \(2019\)](#) for viscosity values of alternate background gases. We plan that future versions of **CARMApy** will include a greater selection of default values as well as schemes for interpolating between them.

2.5. CARMApy Condensates

CARMApy allows for the modeling of pretty much any condensate assuming its material properties are known. To specify a condensate, the density, molar mass, collisional diameter, saturation vapor pressure function, and surface tension function must be known. Each condensate is assumed to condense from a single limiting gas and the molar mass of that gas, the stoichiometry factor of the condensation reaction, and whether or not the condensation reaction is considered a type III reaction (see [C. Helling & P. Woitke \(2006\)](#)) must also be specified. Lastly, if the condensate is formed through heterogeneous nucleation then the cosine of the contact angle between the gas species and the seed particle for the nucleation reaction must be specified.

Symbol	Value	Reference
c_p	1.3×10^8 erg/g/K	T. Kataria et al. (2015)
κ_0	7992.77 ergs/s/cm/K	Fit to E. W. Lemmon (2025)
κ_1	38.08 ergs/s/cm/K ²	
κ_2	-1.2585×10^{-4} ergs/s/cm/K ³	
μ_1	1.7970×10^{-6} poise	D. W. Green & M. Z. Southard (2019), Table 2-138
μ_2	0.685	
μ_3	-0.59 K	
μ_4	140 K ²	

Table 2. CARMapy default parameters for a pure H₂ atmosphere.

It is assumed that the saturation vapor pressure function takes the following form:

$$\log_{10} \frac{p_s}{(10^6 \text{ barye})} = \alpha_0 - \frac{\alpha_1}{T} - \alpha_2[\text{Fe}/\text{H}] - \alpha_3 \log_{10} \frac{P}{(10^6 \text{ barye})} \quad (88)$$

where T is the temperature, P is the atmospheric pressure, and the α_i are coefficients unique to each condensate. Similarly it is assumed the surface tension of the air-condensate boundary, σ takes the following form:

$$\sigma = \sigma_0 + \sigma_1 T \quad (89)$$

where as before, σ_0 and σ_1 are coefficients unique to each condensate.

While still possible to specify, CARMapy defaults to calculating the latent heat of vaporization, L , using the saturation vapor pressures and the Clausius-Clapeyron equation:

$$\frac{d \ln p_s}{dT} = \frac{L}{RT^2} \quad (90)$$

where R is the ideal gas constant.

Lastly, for heterogeneously nucleating species, the contact angle, μ , can be determined through Young’s relation:

$$\mu = \frac{\sigma_{\text{cond}} - \sigma_{\text{interface}}}{\sigma_{\text{core}}} \quad (91)$$

where σ_{cond} is the surface tension of the condensate, σ_{core} is the surface tension of the core, and $\sigma_{\text{interface}}$ is the surface tension of the core-condensate boundary. We most often assume $\sigma_{\text{interface}} = 0$ due to a lack of laboratory measurements.

The values for all the constants assumed for the CARMapy default condensates are given in Appendix B. These constants come from a combination of standard reference databases, density functional theory and molecular dynamics simulations, thermodynamical modeling, and lab experiments. While some of these values are well constrained, a number of them rely on simplifying modeling assumption and/or extrapolation to temperature and pressure regimes far beyond where they were originally contained. Further work constraining the material properties of cloud particles in regimes relevant to exoplanet and brown dwarfs contexts is needed to tamp down on uncertainties in our models.

2.6. Optional Model Initialization Routines

2.6.1. Cloud Base Chemical Equilibrium

CARMA does not include any chemistry calculations other than the cloud microphysics discussed above. This means that a gas will remain at a constant mixing ratio in CARMA in regions that do not contain any cloud particles. Thus, to ensure that the cloud base has an accurate mixing ratio of the gas phase, it is recommended to set the bottom boundary condition for the gas to be a fixed concentration equal to the concentration at the cloud base—CARMapy contains convenience features⁷ that allow the user to easily do precisely this.

After calculating the saturation vapor pressure for the relevant gas species across the provided T - P profile, p'_i , CARMapy uses pyFastChem (J. W. Stock et al. 2022) to calculate the equilibrium partial pressures, p_i of the gas across

⁷ see `carmapy.chemistry.populate_abundances_at_cloud_base()`

those same points. For this process, the cloud base is assumed to form at the location given by equilibrium cloud condensation theory, that is where $p'_i = p_i$. The mixing ratio of the gas at this location (calculated by dividing the partial pressure by the atmospheric pressure) is then set as the boundary condition at the bottom of the atmosphere for the gas.

2.6.2. Adiabatic Atmospheric Extension

It is occasionally useful to extend the atmospheric profile given to higher pressures in order to capture the entirety of the cloud formation process for which we provide a convenience function⁸. To this end, we assume the deep atmosphere is a convective zone and thus follows an adiabatic temperature gradient. The adiabat given by [V. Parmentier et al. \(2015\)](#) which is a fit to [D. Saumon et al. \(1995\)](#) is

$$\nabla_{\text{ad}} = \left(\frac{\partial \ln T}{\partial \ln P} \right)_S = a - bT \quad (92)$$

with $a = 0.32$ and $b = 1/30000 \text{ K}^{-1}$. Assuming we can treat the partial derivatives as total and integrating by partial fractions we arrive at the following equation extrapolating the temperature to any pressure

$$T(P) = \frac{aK(P)}{1 + bK(P)} \quad (93)$$

where

$$K = \frac{T_0}{a - bT_0} \left(\frac{P}{P_0} \right)^a \quad (94)$$

and where (T_0, P_0) is a known T-P point at the bottom of the un-extended atmosphere. The eddy diffusion coefficient can then be extended as $K_{zz} \propto H^{-1/3}$ where $H = kT/\mu m_p g$ is the scale height ([P. Giersch & B. J. Conrath 1985](#), Eqn. 16).

2.7. Post-processing

CARMApy includes built in methods for reading in results and then generating spectra from the simulation output. CARMApy uses `pyFastchem` to calculate equilibrium gas phase abundances to serve as the gas phase input into PICASO ([N. E. Batalha et al. 2019](#))⁹. For the cloud phase

The extinction coefficient, β_{ext} , scattering coefficient, β_{sca} , and the asymmetry parameter, g , for each layer at each wavelength is calculated as follows (Eqns. 12.26 - 12.29, [G. W. Petty 2006](#))

$$\beta_{\text{ext}}(z, \lambda) = \sum_{\text{all cloud species}} \int_0^\infty \pi r^2 n(z) Q_{\text{ext}}(r, \lambda) dr \quad (95)$$

$$\beta_{\text{sca}}(z, \lambda) = \sum_{\text{all cloud species}} \int_0^\infty \pi r^2 n(z) Q_{\text{sca}}(r, \lambda) dr \quad (96)$$

$$g(z, \lambda) = \frac{1}{\beta_{\text{sca}}} \sum_{\text{all cloud species}} \int_0^\infty \pi r^2 n(z) Q_{\text{sca}}(r, \lambda) g(r, \lambda) dr \quad (97)$$

where Q_{ext} and Q_{sca} are the extinction and scattering efficiencies which, along with $g(r, \lambda)$, are calculated using `PyMieScatt` ([B. J. Sumlin et al. 2018](#)). From these values we can easily calculate the single scattering albedo, $\omega = \beta_{\text{sca}}/\beta_{\text{ext}}$, and the optical depth of each layer, $\Delta\tau = \beta_{\text{ext}}\Delta z$, and generate the required cloud phase inputs into PICASO¹⁰. While we do not package PICASO directly into CARMApy as we want to avoid unneeded dependencies, we include in our tutorial sample scripts for generating spectra with CARMApy and PICASO.

2.8. Example Outputs

To demonstrate the use of CARMApy, we first present a minimal example script to run the CARMApy simulation in Figure 2. We additionally present a few example data products producible using the code in Figure 3. Some of

⁸ see `carmapy.Carma.extend_atmosphere()`

⁹ see `carmapy.Results.gen_picaso_atm_file()`

¹⁰ see `carmapy.Results.gen_picaso_cloud_file()`

```

1 import numpy as np
2 import carmapy
3
4 # Sample 2000K Sonora Diamondback Brown Dwarf (Morley+ 2024)
5 P_levels, T_levels, kzz_levels, mu_levels = example_levels()
6
7 carma = Carma("example")
8 carma.set_physical_params(surface_grav=31600, wt_mol=np.mean(mu))
9 carma.set_atmospheric_parameters_from_defaults("Pure H2")
10 carma.set_stepping(dt=100, n_tstep=24000, output_gap=10)
11
12 carma.add_hom_group("TiO2", r_min=1e-8) # Homogeneous TiO2
13 carma.add_het_group("Mg2SiO4", "TiO2", r_min=1e-8 * 2**(1/3)) # Mg2SiO4 on TiO2
14
15 carma.add_P(P_levels)
16 carma.add_T(T_levels)
17 carma.add_kzz(kzz_levels)
18
19 carma.calculate_z(mu_levels)
20 carmapy.chemistry.populate_abundances_at_cloud_base(carma) # invoke fastchem
21
22 carma.run()

```

Figure 2. A minimal CARMApy script which models a 2000 K brown dwarf using the Sonora Diamondback (C. V. Morley et al. 2024) models as input and only TiO₂ and Mg₂SiO₄ condensates

example outputs from CARMApy include a cloud particle size distribution profile derived *a priori* from our microphysical equations (Figure 3, Top Left), the gain and loss rates in each grid cell due to the various microphysical processes (Figure 3, Top Right), spectra generated using PyMieScatt (B. J. Sumlin et al. 2018) and PICASO (N. E. Batalha et al. 2019) (Figure 3, Bottom Left), and the depleted gas abundance profiles caused by cloud formation (Figure 3, Bottom Right). All the 1D examples presented here are based on a 1800 K Brown Dwarf pressure, temperature, and eddy-diffusion structure taken from C. V. Morley et al. (2024) Sample code to generate all these types of figures are available in the tutorials at carmapy.readthedocs.io.

2.9. 2D CARMApy

The functionality to allow for 2D ExoCARMA simulations, which we wrap in CARMApy, was implemented by D. Powell & X. Zhang (2024). In this mode, the longitudinally varying cloud profile is calculated at the equator by advecting the cloud column uniformly around the equator, holding the pressure coordinate of each bin constant while allowing the temperature at each pressure level to vary longitudinally. This process is done in log-pressure coordinates and introduces a vertical metric factor of $ds/dz = T/T_0$ where T_0 is the temperature at the base of the atmosphere (O. B. Toon et al. 1988). The speed of advection is user specified, but typically has been chosen to be the average wind speed at the base of the cloud corresponding to the most relevant homogeneously nucleating condensate. These 2D models are particularly suited to modeling planets which have strong longitudinal asymmetry and stable equatorial jets which dominate the observable region of the planetary atmosphere, such as hot Jupiters (eg. A. P. Showman et al. 2009).

Recent observations of the limb asymmetries between the morning and evening terminators exoplanets show that differing cloud properties play a critical role in explaining the differences in spectra measured at each of these limbs (S. Mukherjee et al. 2026). 2D CARMApy, and the underlying CARMA model, in modeling the cloud column at each longitude, are able to resolve differences in clouds and thus predict limb-asymmetric spectra (see Samra et al. in prep, Kennedy et al. in prep). Additionally this longitude resolution allows us to extract observables such as thermal emission phase curves from our models. Example 2D CARMApy outputs and derived observables, including these limb asymmetric spectra and phase curves, are presented in Figure 4. These outputs were generated using GCM data an

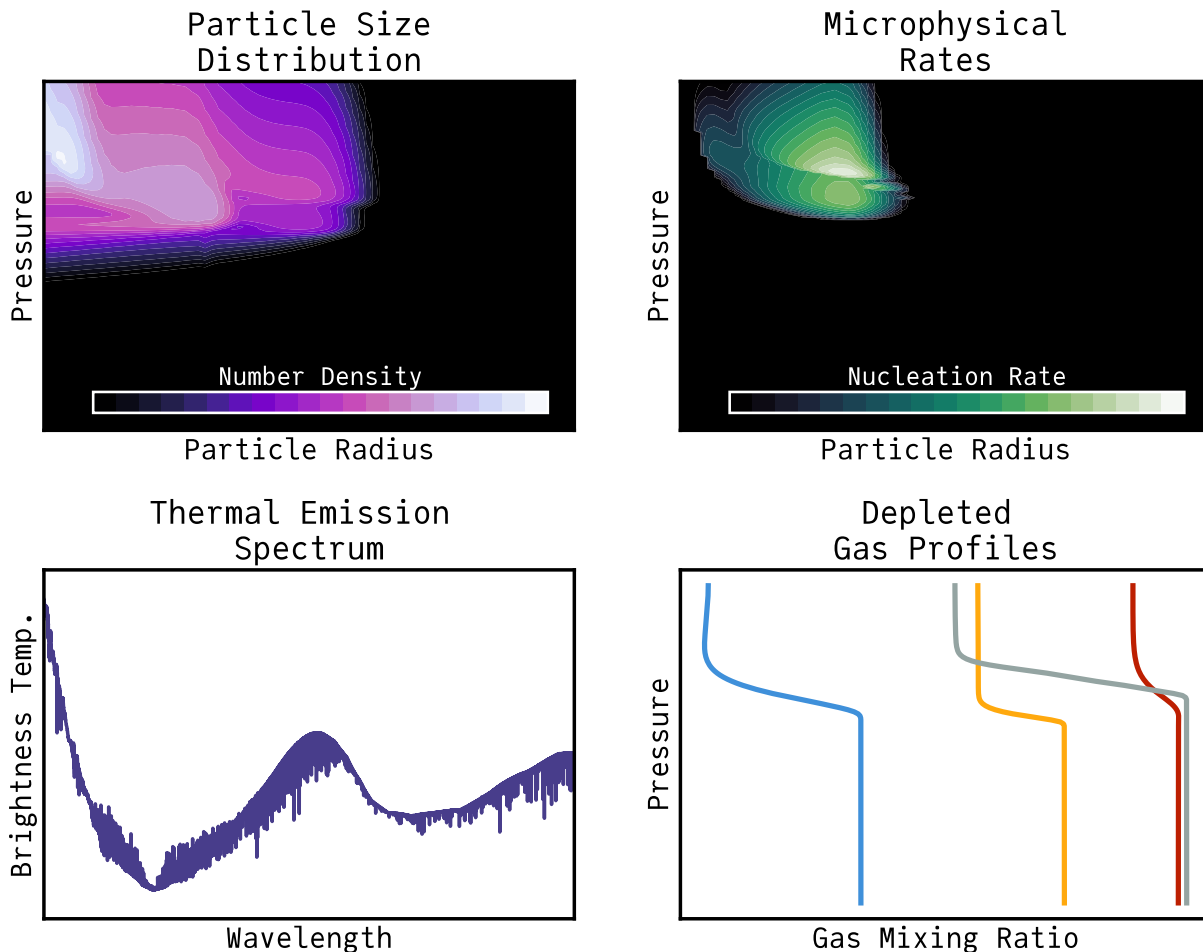


Figure 3. A selection of the data products that can be generated using `CARMaPy`. Axes ticks and color bars are omitted for legibility. Example code to generate all of these type of plots are available in the `CARMaPy` tutorials at carmapy.readthedocs.io **Top Left:** A cloud particle size distribution across the pressure and particle size grid generated by a 1D `CARMaPy` run. **Top Right:** The heterogeneous nucleation rate for the same 1D run. `CARMaPy` is also able to output the homogeneous nucleation rate, the condensational growth rate, and evaporation rate. **Bottom Left:** A thermal emission spectrum generated by a 1D `CARMaPy` run post processed with `PICASO`. **Bottom Right:** The depleted gas abundance profiles generated by a `CARMaPy` run.

1800 K Hot Jupiter from [A. Roth et al. \(2024\)](#). Tutorials showing how these data products are created are available at carmapy.readthedocs.io/en/latest/notebooks/5_2d_carmapy.html.

3. BENCHMARKS

To ensure correctness, we benchmark the results of `CARMaPy` against that of `ExoCARMA 1.0`. For the benchmark, we use a 1-D P-T and eddy-diffusion structure of a 2000 K brown dwarf with $\log g = 4.5$ and $f_{\text{sed}} = 4$ from [C. V. Morley et al. \(2024\)](#). The atmospheric viscosity, thermal conductivity, and specific heat were set to that of a pure H_2 atmosphere¹¹. For this benchmark we initialize a simple nucleation network, allowing TiO_2 to homogeneously condense and allowing Mg_2SiO_4 to heterogeneously condense upon the TiO_2 CCN. The model was run at a timestep of 100 s for 24000 timesteps with minimal I/O to isolate the timing to that of the microphysics calculations. This process took `CARMaPy` ~ 50 seconds on 4 cores or ~ 100 seconds single-threaded on a M4 Macbook Pro. The same process took `ExoCARMA 1.0` ~ 190 seconds on the same test¹².

¹¹ note that the viscosity and thermal conductivity used was not the up-to-date values used as defaults but was instead set to be consistent with ([P. Gao & B. Benneke 2018](#))

¹² Single threaded as OpenMP was not implemented in `ExoCARMA 1.0`

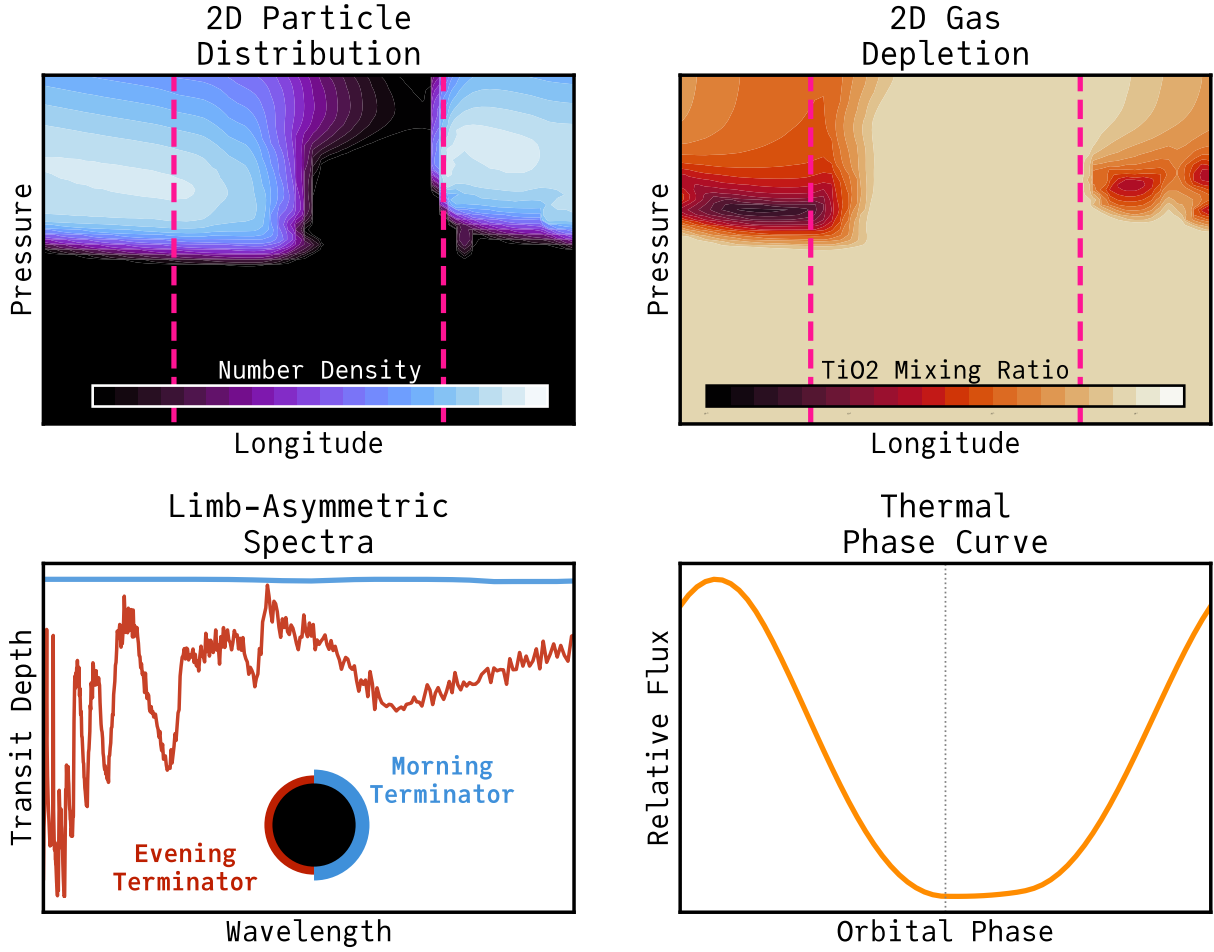


Figure 4. A selection of the data products that can be generated using 2D-CARMApy. Axes ticks and color bars are omitted for legibility. Example code to generate all of these type of plots are available in the CARMApy tutorials at carmapy.readthedocs.io **Top Left:** The 2D cloud particle distribution profile generated by a 2D CARMApy run. The plot is centered on the substellar point and the pink dashed lines are the morning and evening terminators. **Top Right:** The TiO_2 gas abundance profile from a 2D CARMApy run showing the disequilibrium gas depletion caused by cloud formation. The plot is centered on the substellar point and the pink dashed lines are the morning and evening terminators. **Bottom Left:** NIR transmission spectra calculated at the morning (blue) and evening (red) terminators as derived from a 2D CARMApy run. **Bottom Right:** NIR thermal emission phase curve as derived from as 2D CARMApy run.

We then resumed those same simulations with outputting data every 10 timesteps for another 10000 timesteps. We then averaged over these 1000 outputs as CARMA can fluctuate around equilibria but long term averages tend to be stable. The combined TiO_2 and Mg_2SiO_4 particle size distribution profiles are presented Figure 5. These size distributions are, as expected, practically visually indistinguishable. The total cloud and gas mass for each species agrees up to a relative difference $\sim 3 \times 10^{-4}$ and $\sim 3 \times 10^{-5}$ respectively. To get a sense of how these changes impact the observable features of these bodies, we present our analysis of our emission spectra benchmarking in Figure 6. This figure shows the relative difference in the brightness temperature emission spectra between ExoCARMA 1.0 and CARMApy. The maximum absolute error is on the order of 0.3 K which corresponds to a relative error of $\sim 10^{-4}$. At longer wavelengths the maximum absolute error drops to ~ 0.01 K. corresponding to a relative error of $\sim 10^{-5}$. These deviations are of a magnitude which is consistent with floating point error propagated over tens of thousands of timesteps and are small enough to be considered negligible as other assumptions, such as the choice of the eddy-diffusion structure of the atmosphere, will far dominate the uncertainty presented here.

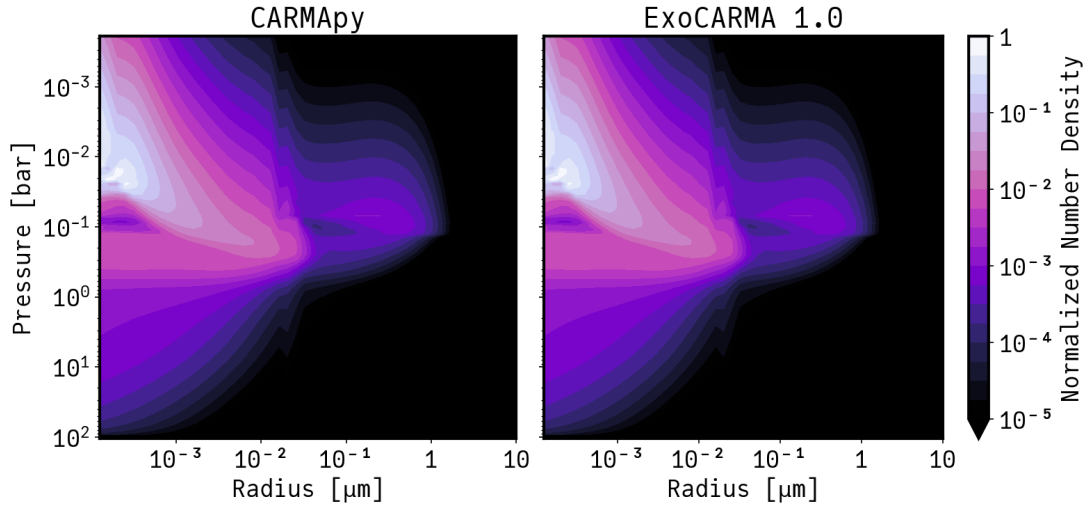


Figure 5. Comparison of the total condensate number density for a sample 2-species 2000 K brown dwarf run, averaged over 1000 samples. The output from `CARMApy` on the left is benchmarked against the `ExoCARMA` code without our edits on the right.

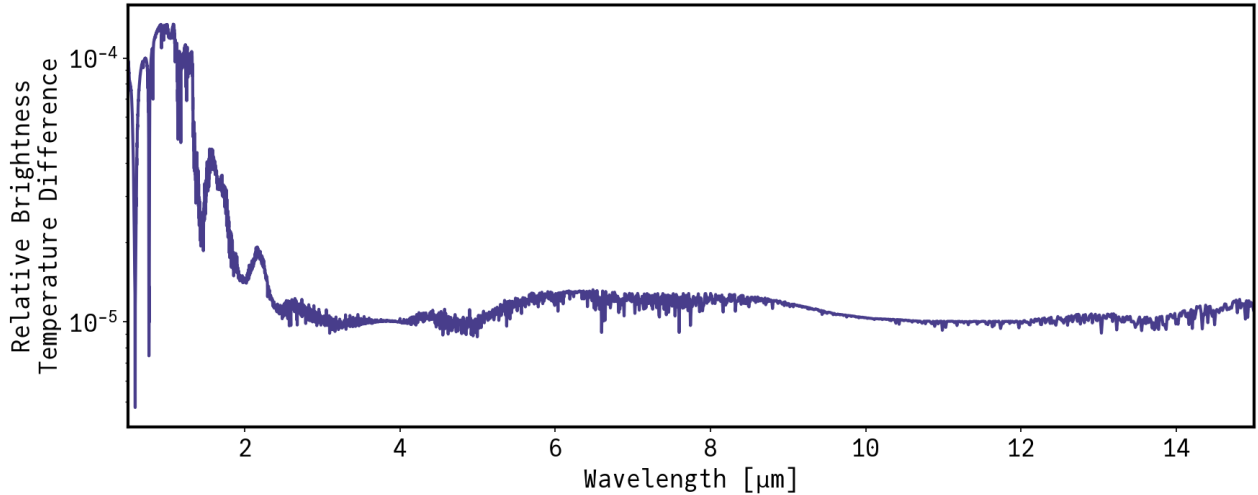


Figure 6. The relative difference in the brightness temperature emission spectra between `ExoCARMA 1.0` and `CARMApy` for a sample 2-species 2000 K brown dwarf run, with number densities averaged over 1000 samples.

4. FUTURE DEVELOPMENT

While `CARMApy` is already an incredibly powerful code, there remains improvements to be made for future releases. Future releases of `CARMApy` likely will include some of the following features:

1. A more complete solution for including hazes, including fractal aggregates and cloud-haze interactions (see Nagpal et al. *in prep*)
2. The ability to have more than one condensate species formed from a single limiting gas (ie. both SiO and SiO_2 forming from SiO gas)
3. Radiatively active clouds
4. Coupling with gas phase chemistry
5. Expanding the number of default atmospheric parameters and condensates available with `CARMApy`

As we continue to use and refine `CARMApy` the solutions we develop will be released to the same channels as described herein.

5. CONCLUSIONS

Here we have presented the new python-based bin-scheme microphysical cloud model `CARMApy`, as well as an update to the underlying Fortran code, `ExoCARMA 2.0`. `CARMApy` is pip installable, is available on GitHub,¹³ and has tutorials and documentation hosted at carmapy.readthedocs.io. The code and related documentation are also archived with Zenodo.¹⁴

In addition to detailed microphysical modeling of exoplanets in both 1D and 2D, `CARMApy` includes a number of features to help with the initialization and analysis of the model. Interfaces with `pyFastchem` provide for straightforward setting of chemical equilibrium abundances. Similarly, we provide post-processing code that exposes the simulation results in an intuitive interface, allows for quick plotting of size distributions, microphysical rates, and depleted gas profiles, and allows for fast and simple post-processing the output of the simulations into spectra with `PICASO`. `CARMApy` also exposes interfaces such that the user is able to easily change the condensates included in the model as well as change the background atmospheric parameters. We have benchmarked our code against the old version of the Fortran code `ExoCARMA 1.0` and find the our updated code is able to reproduce the results of the old code to within some negligible deviations, while running ~ 1.9 times faster single threaded and ~ 3.8 times faster multithreaded.

ACKNOWLEDGMENTS

The authors would like to thank Thomas Kennedy for helping beta test this code. LLM tools (Sonnet 4.6, Opus 4.7-4.8) were used to format tables, to help implement and guide reasoning about code, and to suggest phrasing of sentences during preparation of this manuscript. This work benefited from the 2025 Exoplanet Summer Program in the Other Worlds Laboratory (OWL) at the University of California, Santa Cruz, a program funded by the Heising-Simons Foundation and NASA. X.Z. acknowledges support from the NSF grant (AST2307463), NASA Exoplanet Research grant (80NSSC22K0236), and the NASA Interdisciplinary Consortia for Astrobiology Research grant (80NSSC21K0597). VN acknowledges support from the National Science Foundation Graduate Research Fellowship under Grant No. DGE 2140001. D.S. acknowledges funding as part of JWST GO program 3969 (PIs: Espinoza, Powell).

AUTHOR CONTRIBUTIONS

WC led the writing of this paper, contributed to the development of `ExoCARMA`, and conceived of and led the development of the `CARMApy` wrapper. DP co-lead the development of `ExoCARMA` and supervised the writing of this paper and the development of the `CARMApy` wrapper. XZ supervised and contributed to the development of `ExoCARMA`, supervised the development of the `CARMApy` wrapper, and helped edit this paper. PG co-lead the development of `ExoCARMA` and helped edit this paper. DS and VN both contributed to the development of the `CARMApy` wrapper and helped edit this paper.

Software: `numpy` (C. R. Harris et al. 2020), `matplotlib` (J. D. Hunter 2007), `scipy` (P. Virtanen et al. 2020), `pyfastchem` (J. W. Stock et al. 2022), `PyMieScatt` (B. J. Sumlin et al. 2018), `PICASO` (N. E. Batalha et al. 2019)

REFERENCES

- | | |
|---|--|
| Ackerman, A. S., & Marley, M. S. 2001, <i>The Astrophysical Journal</i> , 556, 872, doi: 10.1086/321540 | Barth, E. 2020, <i>Atmosphere</i> , 11, 1064, doi: 10.3390/atmos11101064 |
| Bardeen, C. G., Toon, O. B., Jensen, E. J., Marsh, D. R., & Harvey, V. L. 2008, <i>Journal of Geophysical Research: Atmospheres</i> , 113, doi: 10.1029/2007JD009515 | Barth, E. L., & Toon, O. B. 2003, <i>Icarus</i> , 162, 94, doi: 10.1016/S0019-1035(02)00067-2 |
| | Barth, E. L., & Toon, O. B. 2004, <i>Geophysical Research Letters</i> , 31, L17S07, doi: 10.1029/2004GL019825 |
| | Barth, E. L., & Toon, O. B. 2006, <i>Icarus</i> , 182, 230, doi: 10.1016/j.icarus.2005.12.017 |

¹³ <https://github.com/wcukier/carmapy>

¹⁴ <https://doi.org/10.5281/zenodo.20433610>

- Batalha, N. E., Marley, M. S., Lewis, N. K., & Fortney, J. J. 2019, *The Astrophysical Journal*, 878, 70, doi: [10.3847/1538-4357/ab1b51](https://doi.org/10.3847/1538-4357/ab1b51)
- Beard, K. V., & Ochs III, H. T. 1984, *Journal of Geophysical Research: Atmospheres*, 89, 7165, doi: [10.1029/JD089iD05p07165](https://doi.org/10.1029/JD089iD05p07165)
- Begemann, B., Dorschner, J., Henning, T., et al. 1997, *The Astrophysical Journal*, 476, 199, doi: [10.1086/303597](https://doi.org/10.1086/303597)
- Burningham, B., Faherty, J. K., Gonzales, E. C., et al. 2021, Cloud busting: enstatite and quartz clouds in the atmosphere of 2M2224-0158, doi: [10.48550/arXiv.2105.04268](https://doi.org/10.48550/arXiv.2105.04268)
- Calamari, E., Faherty, J. K., Visscher, C., et al. 2024, *The Astrophysical Journal*, 963, 67, doi: [10.3847/1538-4357/ad1f6d](https://doi.org/10.3847/1538-4357/ad1f6d)
- Chen, Z., Bhartia, P. K., Loughman, R., Colarco, P., & DeLand, M. 2018, *Atmospheric Measurement Techniques*, 11, 6495, doi: [10.5194/amt-11-6495-2018](https://doi.org/10.5194/amt-11-6495-2018)
- Colaprete, A., Toon, O. B., & Magalhães, J. A. 1999, *Journal of Geophysical Research*, 104, 9043, doi: [10.1029/1998JE900018](https://doi.org/10.1029/1998JE900018)
- Colella, P., & Woodward, P. R. 1984, *Journal of Computational Physics*, 54, 174, doi: [10.1016/0021-9991\(84\)90143-8](https://doi.org/10.1016/0021-9991(84)90143-8)
- Dagum, L., & Menon, R. 1998, *IEEE Computational Science and Engineering*, 5, 46, doi: [10.1109/99.660313](https://doi.org/10.1109/99.660313)
- Di Girolamo, L., Zhao, G., Zhang, G., et al. 2025, *Nature*, 643, 983, doi: [10.1038/s41586-025-09242-1](https://doi.org/10.1038/s41586-025-09242-1)
- Dobrovinskaya, E. R., Lytvynov, L. A., & Pishchik, V. 2009, in *Sapphire: Material, Manufacturing, Applications*, ed. V. Pishchik, L. A. Lytvynov, & E. R. Dobrovinskaya (Boston, MA: Springer US), 55–176, doi: [10.1007/978-0-387-85695-7_2](https://doi.org/10.1007/978-0-387-85695-7_2)
- Durran, D. R. 1999, *Numerical methods for wave equations in geophysical fluid dynamics*, Texts in applied mathematics No. 32 (New York: Springer)
- Friedlander, S. K. 1957, *AIChE Journal*, 3, 43, doi: [10.1002/aic.690030109](https://doi.org/10.1002/aic.690030109)
- Fuchs, N. 1951, *Dokl. Akad. Nauk SSSR*, 81, 1043
- Fuchs, N. A. 1964, *The mechanics of aerosols*, rev. and enl. edn. (New York: Macmillan). <https://catalog.lib.uchicago.edu/vufind/Record/2243096?sid=75262889>
- Gail, H.-P., Wetzell, S., Pucci, A., & Tamanai, A. 2013, *Astronomy & Astrophysics*, 555, A119, doi: [10.1051/0004-6361/201321807](https://doi.org/10.1051/0004-6361/201321807)
- Gao, P. 2017, Ph.D., California Institute of Technology, United States – California, doi: [10.7907/Z99W0CGS](https://doi.org/10.7907/Z99W0CGS)
- Gao, P., & Benneke, B. 2018, *The Astrophysical Journal*, 863, 165, doi: [10.3847/1538-4357/aad461](https://doi.org/10.3847/1538-4357/aad461)
- Gao, P., & Powell, D. 2021, *The Astrophysical Journal Letters*, 918, L7, doi: [10.3847/2041-8213/ac139f](https://doi.org/10.3847/2041-8213/ac139f)
- Gao, P., Zhang, X., Crisp, D., Bardeen, C. G., & Yung, Y. L. 2014, *Icarus*, 231, 83, doi: [10.1016/j.icarus.2013.10.013](https://doi.org/10.1016/j.icarus.2013.10.013)
- Gao, P., Fan, S., Wong, M. L., et al. 2017, *Icarus*, 287, 116, doi: [10.1016/j.icarus.2016.09.030](https://doi.org/10.1016/j.icarus.2016.09.030)
- Gao, P., Thorngren, D. P., Lee, E. K. H., et al. 2020, *Nature Astronomy*, 4, 951, doi: [10.1038/s41550-020-1114-3](https://doi.org/10.1038/s41550-020-1114-3)
- Gao, P., Piette, A. A. A., Steinrueck, M. E., et al. 2023, *The Astrophysical Journal*, 951, 96, doi: [10.3847/1538-4357/acd16f](https://doi.org/10.3847/1538-4357/acd16f)
- Gierasch, P., & Conrath, B. J. 1985, in *Recent advances in planetary meteorology: the Seymour Hess memorial symposium – IUGG general assembly Hamburg, 18-19 August 1983*, ed. G. E. Hunt (Cambridge London New York [etc.]: Cambridge university press)
- Glasser, L., & Jenkins, H. D. B. 2000, *Journal of the American Chemical Society*, 122, 632, doi: [10.1021/ja992375u](https://doi.org/10.1021/ja992375u)
- Green, D. W., & Southard, M. Z. 2019, *Perry's Chemical Engineers' Handbook*, 9th Edition, 9th edn. (New York, N.Y: McGraw-Hill Education)
- Güttler, C., Blum, J., Zsom, A., Ormel, C. W., & Dullemond, C. P. 2010, *Astronomy and Astrophysics*, 513, A56, doi: [10.1051/0004-6361/200912852](https://doi.org/10.1051/0004-6361/200912852)
- Harris, C. R., Millman, K. J., van der Walt, S. J., et al. 2020, *Nature*, 585, 357, doi: [10.1038/s41586-020-2649-2](https://doi.org/10.1038/s41586-020-2649-2)
- Hasegawa, T. I., Herbst, E., & Leung, C. M. 1992, *The Astrophysical Journal Supplement Series*, 82, 167, doi: [10.1086/191713](https://doi.org/10.1086/191713)
- Helling, C., Oevermann, M., Lüttke, M. J. H., Klein, R., & Sedlmayr, E. 2001, *Astronomy & Astrophysics*, 376, 194, doi: [10.1051/0004-6361:20010937](https://doi.org/10.1051/0004-6361:20010937)
- Helling, C., & Woitke, P. 2006, *Astronomy and Astrophysics*, Volume 455, Issue 1, August III 2006, pp.325-338, 455, 325, doi: [10.1051/0004-6361:20054598](https://doi.org/10.1051/0004-6361:20054598)
- Helling, C., Lee, G., Dobbs-Dixon, I., et al. 2016, *Monthly Notices of the Royal Astronomical Society*, 460, 855, doi: [10.1093/mnras/stw662](https://doi.org/10.1093/mnras/stw662)
- Honsberg, C. B., & Bowden, S. G. 2007, *MnS*, <https://www.pveducation.org/pvc/drom/materials/MnS>
- Huffman, D. R., & Wild, R. L. 1967, *Physical Review*, 156, 989, doi: [10.1103/PhysRev.156.989](https://doi.org/10.1103/PhysRev.156.989)
- Hunter, J. D. 2007, *Computing in Science & Engineering*, 9, 90, doi: [10.1109/MCSE.2007.55](https://doi.org/10.1109/MCSE.2007.55)
- Jacobson, M. Z. 2005, *Fundamentals of atmospheric modeling*, 2nd edn. (Cambridge (GB): Cambridge University Press)

- Jacobson, M. Z., Turco, R. P., Jensen, E. J., & Toon, O. B. 1994, *Atmospheric Environment*, 28, 1327, doi: [10.1016/1352-2310\(94\)90280-1](https://doi.org/10.1016/1352-2310(94)90280-1)
- Jäger, C., Dorschner, J., Mutschke, H., Posch, T., & Henning, T. 2003, *Astronomy & Astrophysics*, 408, 193, doi: [10.1051/0004-6361:20030916](https://doi.org/10.1051/0004-6361:20030916)
- Kataria, T., Showman, A. P., Fortney, J. J., et al. 2015, *The Astrophysical Journal*, 801, 86, doi: [10.1088/0004-637X/801/2/86](https://doi.org/10.1088/0004-637X/801/2/86)
- Kaye, G. W. C., & Laby, T. H. 2005, in *Tables of Physical and Chemical Constants and Some Mathematical Functions* (Kaye & Laby Online. Version 1.0). <https://web.archive.org/web/20190506031327/http://www.kayelaby.npl.co.uk/>
- Khachai, H., Khenata, R., Bouhemadou, A., et al. 2009, *Journal of Physics Condensed Matter*, 21, 095404, doi: [10.1088/0953-8984/21/9/095404](https://doi.org/10.1088/0953-8984/21/9/095404)
- Kitzmann, D., & Heng, K. 2018, *Monthly Notices of the Royal Astronomical Society*, 475, 94, doi: [10.1093/mnras/stx3141](https://doi.org/10.1093/mnras/stx3141)
- Koike, C., Kaito, C., Yamamoto, T., et al. 1995, *Icarus*, 114, 203, doi: [10.1006/icar.1995.1055](https://doi.org/10.1006/icar.1995.1055)
- Kozasa, T., Hasegawa, H., & Nomoto, K. 1989, *The Astrophysical Journal*, 344, 325, doi: [10.1086/167801](https://doi.org/10.1086/167801)
- Langmuir, I. 1948, *Journal of the Atmospheric Sciences*, 5, 175, doi: [10.1175/1520-0469\(1948\)005<0175:TPORBA>2.0.CO;2](https://doi.org/10.1175/1520-0469(1948)005<0175:TPORBA>2.0.CO;2)
- Lee, E., Helling, C., Giles, H., & Bromley, S. T. 2015, *Astronomy & Astrophysics*, 575, A11, doi: [10.1051/0004-6361/201424621](https://doi.org/10.1051/0004-6361/201424621)
- Lee, E. K. H., & Ohno, K. 2025a, Three-dimensional dynamical evolution of cloud particle microphysics in sub-stellar atmospheres I. Description and exploring Y-dwarf atmospheric variability, arXiv, doi: [10.48550/arXiv.2411.10305](https://doi.org/10.48550/arXiv.2411.10305)
- Lee, E. K. H., & Ohno, K. 2025b, *Astronomy and Astrophysics*, 704, A319, doi: [10.1051/0004-6361/202556451](https://doi.org/10.1051/0004-6361/202556451)
- Lee, E. K. H., Wardenier, J. P., Prinoth, B., et al. 2022, *The Astrophysical Journal*, 929, 180, doi: [10.3847/1538-4357/ac61d6](https://doi.org/10.3847/1538-4357/ac61d6)
- Lemmon, E. W. 2025, in *CRC Handbook of chemistry and physics*, 106th edn., ed. J. R. Rumble, T. J. Bruno, D. R. Burgess, & L. R. McEwen, CRC handbook of chemistry and physics / Chemical Rubber Company No. 106th edition (2025) (Boca Raton London New York: CRC Press, Taylor & Francis Group)
- Lian, S., Zhou, L., Murphy, D. M., et al. 2022, *Atmospheric Chemistry & Physics*, 22, 13659, doi: [10.5194/acp-22-13659-2022](https://doi.org/10.5194/acp-22-13659-2022)
- Lynch, D., & Hunter, W. R. 1997, in *Handbook of Optical Constants of Solids* (Academic Press), 341–419, doi: [10.1016/B978-012544415-6.50057-1](https://doi.org/10.1016/B978-012544415-6.50057-1)
- MacDonald, R. J. 2023, *The Journal of Open Source Software*, 8, 4873, doi: [10.21105/joss.04873](https://doi.org/10.21105/joss.04873)
- MacDonald, R. J., & Madhusudhan, N. 2017, *Monthly Notices of the Royal Astronomical Society*, 469, 1979, doi: [10.1093/mnras/stx804](https://doi.org/10.1093/mnras/stx804)
- Malsky, I., Rauscher, E., Roman, M. T., et al. 2024, *The Astrophysical Journal*, 961, 66, doi: [10.3847/1538-4357/ad0b70](https://doi.org/10.3847/1538-4357/ad0b70)
- Mang, J., Gao, P., Hood, C. E., et al. 2022, *The Astrophysical Journal*, 927, 184, doi: [10.3847/1538-4357/ac51d3](https://doi.org/10.3847/1538-4357/ac51d3)
- Mang, J., Morley, C. V., Robinson, T. D., & Gao, P. 2024, *The Astrophysical Journal*, 974, 190, doi: [10.3847/1538-4357/ad6c4c](https://doi.org/10.3847/1538-4357/ad6c4c)
- Marley, M. S., Saumon, D., Visscher, C., et al. 2021, *The Astrophysical Journal*, 920, 85, doi: [10.3847/1538-4357/ac141d](https://doi.org/10.3847/1538-4357/ac141d)
- Michelangeli, D. V., Toon, O. B., Haberle, R. M., & Pollack, J. B. 1993, *Icarus*, 102, 261, doi: [10.1006/icar.1993.1048](https://doi.org/10.1006/icar.1993.1048)
- Mollière, P., Stolker, T., Lacour, S., et al. 2020, *Astronomy & Astrophysics*, 640, A131, doi: [10.1051/0004-6361/202038325](https://doi.org/10.1051/0004-6361/202038325)
- Montaner, A., Galtier, M., Benoit, C., & Bill, H. 1979, *Physica Status Solidi Applied Research*, 52, 597, doi: [10.1002/pssa.2210520228](https://doi.org/10.1002/pssa.2210520228)
- Morley, C. V., Fortney, J. J., Marley, M. S., et al. 2012, *The Astrophysical Journal*, 756, 172, doi: [10.1088/0004-637X/756/2/172](https://doi.org/10.1088/0004-637X/756/2/172)
- Morley, C. V., Mukherjee, S., Marley, M. S., et al. 2024, *The Sonora Substellar Atmosphere Models. III. Diamondback: Atmospheric Properties, Spectra, and Evolution for Warm Cloudy Substellar Objects*, arXiv, doi: [10.48550/arXiv.2402.00758](https://doi.org/10.48550/arXiv.2402.00758)
- Mukherjee, S., Sing, D. K., Fu, G., et al. 2026, *Science*, 392, 858, doi: [10.1126/science.adx5903](https://doi.org/10.1126/science.adx5903)
- Ohno, K., & Okuzumi, S. 2017, *The Astrophysical Journal*, 835, 261, doi: [10.3847/1538-4357/835/2/261](https://doi.org/10.3847/1538-4357/835/2/261)
- Palik, E. D. 1985, *Academic Press Handbook Series*. <https://ui.adsabs.harvard.edu/abs/1985hocs.book....P/abstract>
- Parmentier, V., Guillot, T., Fortney, J. J., & Marley, M. S. 2015, *Astronomy & Astrophysics*, 574, A35, doi: [10.1051/0004-6361/201323127](https://doi.org/10.1051/0004-6361/201323127)
- Parmentier, V., Showman, A. P., & Fortney, J. J. 2021, *Monthly Notices of the Royal Astronomical Society*, 501, 78, doi: [10.1093/mnras/staa3418](https://doi.org/10.1093/mnras/staa3418)

- Petrus, S., Whiteford, N., Patapis, P., et al. 2024, The JWST Early Release Science Program for Direct Observations of Exoplanetary Systems V: Do Self-Consistent Atmospheric Models Represent JWST Spectra? A Showcase With VHS 1256 b, arXiv, doi: [10.48550/arXiv.2312.03852](https://doi.org/10.48550/arXiv.2312.03852)
- Petty, G. W. 2006, A first course in atmospheric radiation, 2nd edn. (Madison, Wis: Sundog Pub)
- Phillip, H. R. 1997, in Handbook of Optical Constants of Solids (Academic Press), 765–769, doi: [10.1016/B978-012544415-6.50039-X](https://doi.org/10.1016/B978-012544415-6.50039-X)
- Plummer, M. K., Cocchini, F. P., Kearns, P. A., et al. 2025, Mapping the Cloud-Driven Atmospheric Dynamics & Chemistry of an Isolated Exoplanet Analog with Harmonic Signatures, arXiv, doi: [10.48550/arXiv.2510.02260](https://doi.org/10.48550/arXiv.2510.02260)
- Powell, D., Loudon, T., Kreidberg, L., et al. 2019a, The Astrophysical Journal, 887, 170, doi: [10.3847/1538-4357/ab55d9](https://doi.org/10.3847/1538-4357/ab55d9)
- Powell, D., Murray-Clay, R., Pérez, L. M., Schlichting, H. E., & Rosenthal, M. 2019b, The Astrophysical Journal, 878, 116, doi: [10.3847/1538-4357/ab20ce](https://doi.org/10.3847/1538-4357/ab20ce)
- Powell, D., & Zhang, X. 2024, The Astrophysical Journal, 969, 5, doi: [10.3847/1538-4357/ad3de4](https://doi.org/10.3847/1538-4357/ad3de4)
- Powell, D., Zhang, X., Gao, P., & Parmentier, V. 2018, The Astrophysical Journal, 860, 18, doi: [10.3847/1538-4357/aac215](https://doi.org/10.3847/1538-4357/aac215)
- Pruppacher, H., & Klett, J. 2010, Atmospheric and Oceanographic Sciences Library, Vol. 18, Microphysics of Clouds and Precipitation, ed. L. A. Mysak & K. Hamilton (Dordrecht: Springer Netherlands), doi: [10.1007/978-0-306-48100-0](https://doi.org/10.1007/978-0-306-48100-0)
- Querry, M. R. 1987, Optical constants of minerals and other materials from the millimeter to the ultraviolet (Aberdeen Proving Ground, Md: Chemical Research, Development & Engineering Center, U.S. Army Armament Munitions Chemical Command)
- Rakic, A. D., Djuricic, A. B., Elazar, J. M., & Majewski, M. L. 1998, Applied Optics, 37, 5271, doi: [10.1364/AO.37.005271](https://doi.org/10.1364/AO.37.005271)
- Ribarsky, M. W. 1997, in Handbook of Optical Constants of Solids (Academic Press), 795–804, doi: [10.1016/B978-012544415-6.50042-X](https://doi.org/10.1016/B978-012544415-6.50042-X)
- Roth, A., Parmentier, V., & Hammond, M. 2024, Large Grid of Non-Grey Global Circulation Models Run With SPARC/MiTgcm, Zenodo, doi: [10.5281/zenodo.10960010](https://doi.org/10.5281/zenodo.10960010)
- Rusch, D., Thomas, G., Merkel, A., et al. 2017, Journal of Atmospheric and Solar-Terrestrial Physics, 162, 97, doi: [10.1016/j.jastp.2016.04.018](https://doi.org/10.1016/j.jastp.2016.04.018)
- Samra, D., Helling, C., & Birnstiel, T. 2022, Astronomy and Astrophysics, 663, A47, doi: [10.1051/0004-6361/202142651](https://doi.org/10.1051/0004-6361/202142651)
- Sanderson, R. T. 1976, Chemical bonds and bond energy, 2nd edn., Physical chemistry, a series of monographs No. v. 21 (New York: Academic Press)
- Saumon, D., Chabrier, G., & Van Horn, H. M. 1995, The Astrophysical Journal Supplement Series, 99, 713, doi: [10.1086/192204](https://doi.org/10.1086/192204)
- Sedlmayr, E., & Gail, H.-P. 2014, Physics and chemistry of circumstellar dust shells, Cambridge astrophysics series No. 52 (New York: Cambridge university press)
- Seinfeld, J. H., & Pandis, S. N. 1998, Atmospheric chemistry and physics: from air pollution to climate change (New York: Wiley)
- Showman, A. P., Cho, J. Y.-K., & Menou, K. 2009, Atmospheric Circulation of Exoplanets, arXiv, doi: [10.48550/arXiv.0911.3170](https://doi.org/10.48550/arXiv.0911.3170)
- Stock, J. W., Kitzmann, D., & Patzer, A. B. C. 2022, Monthly Notices of the Royal Astronomical Society, 517, 4070, doi: [10.1093/mnras/stac2623](https://doi.org/10.1093/mnras/stac2623)
- Sumlin, B. J., Heinson, W. R., & Chakrabarty, R. K. 2018, Journal of Quantitative Spectroscopy and Radiative Transfer, 205, 127, doi: [10.1016/j.jqsrt.2017.10.012](https://doi.org/10.1016/j.jqsrt.2017.10.012)
- Tielens, A. G. G. M., & Allamandola, L. J. 1987, in Interstellar Processes, Vol. 134, 397, doi: [10.1007/978-94-009-3861-8_16](https://doi.org/10.1007/978-94-009-3861-8_16)
- Tilmes, S., Mills, M. J., Zhu, Y., et al. 2023, Description and performance of the CARMA sectional aerosol microphysical model in CESM2, Atmospheric sciences, doi: [10.5194/gmd-2023-79](https://doi.org/10.5194/gmd-2023-79)
- Toon, O. B., Turco, R. P., Westphal, D., Malone, R., & Liu, M. 1988, https://journals.ametsoc.org/view/journals/atsc/45/15/1520-0469_1988_045_2123_ammfad_2_0_co_2.xml
- Turco, R. P., Hamill, P., Toon, O. B., Whitten, R. C., & Kiang, C. S. 1979, Journal of the Atmospheric Sciences, 36, 699, doi: [10.1175/1520-0469\(1979\)036<0699:AODMDA>2.0.CO;2](https://doi.org/10.1175/1520-0469(1979)036<0699:AODMDA>2.0.CO;2)
- Vehkamäki, H., Määttänen, A., Lauri, A., Napari, I., & Kulmala, M. 2007, Atmospheric Chemistry and Physics, 7, 309, doi: [10.5194/acp-7-309-2007](https://doi.org/10.5194/acp-7-309-2007)
- Virtanen, P., Gommers, R., Oliphant, T. E., et al. 2020, Nature Methods, 17, 261, doi: [10.1038/s41592-019-0686-2](https://doi.org/10.1038/s41592-019-0686-2)
- Visscher, C., Lodders, K., & Bruce Fegley, J. 2006, The Astrophysical Journal, 648, 1181, doi: [10.1086/506245](https://doi.org/10.1086/506245)
- Wakeford, H. R., & Sing, D. K. 2015, Astronomy and Astrophysics, 573, A122, doi: [10.1051/0004-6361/201424207](https://doi.org/10.1051/0004-6361/201424207)

- Wakeford, H. R., Visscher, C., Lewis, N. K., et al. 2017, Monthly Notices of the Royal Astronomical Society, 464, 4247, doi: [10.1093/mnras/stw2639](https://doi.org/10.1093/mnras/stw2639)
- Wetzel, S., Klevenz, M., Gail, H.-P., Pucci, A., & Tieloff, M. 2013, Astronomy and Astrophysics, 553, A92, doi: [10.1051/0004-6361/201220803](https://doi.org/10.1051/0004-6361/201220803)
- Woitke, P., & Helling, C. 2003, Astronomy and Astrophysics, 399, 297, doi: [10.1051/0004-6361:20021734](https://doi.org/10.1051/0004-6361:20021734)
- Woitke, P., & Helling, C. 2004, Astronomy & Astrophysics, 414, 335, doi: [10.1051/0004-6361:20031605](https://doi.org/10.1051/0004-6361:20031605)
- Woitke, P., Helling, C., & Gunn, O. 2020, Astronomy and Astrophysics, 634, A23, doi: [10.1051/0004-6361/201936281](https://doi.org/10.1051/0004-6361/201936281)
- Wolf, E., Kopparapu, R., Haqq-Misra, J., & Fauchez, T. J. 2022, ExoCAM: A 3D Climate Model for Exoplanet Atmospheres, arXiv, doi: [10.48550/arXiv.2201.09797](https://doi.org/10.48550/arXiv.2201.09797)
- Xue, Q., Bean, J. L., Zhang, M., et al. 2024, The Astrophysical Journal Letters, 963, L5, doi: [10.3847/2041-8213/ad2682](https://doi.org/10.3847/2041-8213/ad2682)
- Zack, L. N., & Ziurys, L. M. 2009, Journal of Molecular Spectroscopy, 257, 213, doi: [10.1016/j.jms.2009.08.009](https://doi.org/10.1016/j.jms.2009.08.009)
- Zeidler, S., Posch, T., Mutschke, H., Richter, H., & Wehrhan, O. 2011, Astronomy & Astrophysics, 526, A68, doi: [10.1051/0004-6361/201015219](https://doi.org/10.1051/0004-6361/201015219)
- Zeldovich, Y. B., Granik, A., Jackson, E., et al. 1992, in Selected works of Yakov Borisovich Zeldovich (Princeton (N.J.): Princeton university press)
- Zhang, H., Huang, F., Gilbert, B., & Banfield, J. F. 2003, The Journal of Physical Chemistry B, 107, 13051, doi: [10.1021/jp036108t](https://doi.org/10.1021/jp036108t)

APPENDIX

A. TABLE OF VARIABLES

Table 3. Summary of variables used in this work.

Symbol	Description
a_c	Critical radius for nucleation
A_k	Kelvin factor
$\alpha_0, \alpha_1, \alpha_2, \alpha_3$	Coefficients of the saturation vapor pressure fit
β	Interpolation factor between continuum and kinetic coagulation regimes
B_0, \dots, B_6	Empirical coefficients for the polynomial fit of Re as a function of the Best number (Table 1)
c_p	Specific heat capacity of the atmosphere
c_{surf}	Surface number density of condensate molecules on the CCN
C_c	Cunningham slip factor
C_D	Drag coefficient
d_q	Collision diameter of the limiting gas molecule
D_i	Brownian diffusion coefficient of particle species i
D_v	Molecular diffusion coefficient of the condensate vapor
D'_v	Corrected molecular diffusion coefficient
δ_i	Transitional length scale for particle i in the coagulation regime interpolation
ΔF_c	Free energy of formation of a critical nucleus
$\Delta F'_c$	Second derivative of ΔF_c w.r.t. molecule number, evaluated at a_c
E_A	Collision efficiency in the aerodynamic limit ($Re \gg 1$)
E_{coalesce}	Coalescence (sticking) efficiency
E_{collide}	Collision efficiency for gravitational coalescence
E_{Fuchs}	Fuchs collision efficiency, correcting E_{Langmuir} for direct interception by finite-size particles
E_{Langmuir}	Langmuir collision efficiency
E_V	Collision efficiency in the viscous limit ($Re \ll 1$)
η_a	Kinematic viscosity of the atmosphere
f	Shape factor relating heterogeneous to homogeneous free energy of formation
f_r	Particle mixing ratio
f_{sed}	Sedimentation efficiency parameter (equilibrium cloud condensation models)
[Fe/H]	Atmospheric metallicity
F_{ad}	Advective flux across a bin boundary
F_{des}	Desorption energy of the condensate molecule from the CCN
F_{dif}	Diffusive flux across a bin boundary
F_t	Thermal ventilation factor
F_v	Mass ventilation factor
g	Gravitational acceleration
g_m	Number of molecules in a particle of radius a_c

Table 3 continued on next page

Table 3 (*continued*)

Symbol	Description
H	Atmospheric pressure scale height, $H = kT/\mu m_p g$
J_{het}	Heterogeneous nucleation rate
J_{hom}	Homogeneous nucleation rate
J_{ki}	Heterogeneous nucleation rate producing bin- k particles on bin- i CCN
k	Boltzmann constant
K_{12}^B	Brownian coagulation kernel
K_{12}^{DE}	Convective diffusion enhancement coagulation kernel
K_{12}^G	Gravitational collection coagulation kernel
K_{12}^{tot}	Total coagulation kernel
K_{zz}	Eddy (turbulent) diffusion coefficient
κ_a	Thermal conductivity of the atmosphere
κ'_a	Corrected atmospheric thermal conductivity
$\kappa_0, \kappa_1, \kappa_2$	Coefficients for the thermal conductivity parameterization
Kn	Knudsen number for transport
Kn_c	Collisional Knudsen number of the condensing gas
Kn_t	Thermal Knudsen number of the condensing gas
L	Latent heat of vaporization; also the loss rate in the semi-implicit coagulation/growth update
ℓ, ℓ_c, ℓ_t	Mean free paths associated with Kn , Kn_c , and Kn_t , respectively
ℓ_i	Mean free path of particle i
λ_c, λ_t	Correction coefficients for D'_v and κ'_a
m	Mass of a cloud particle
m_i	Mass of particles in bin i
m_{i+j}	Combined mass of two coagulating particles, $m_{i+j} = m_i + m_j$
m_p	Proton mass
m_v	Mass of a condensate gas particle
M	Molar mass of the condensate
M_a	Mean molar mass of the background atmosphere
M_v	Molar mass of the limiting (key) gas species
μ	Cosine of the contact angle between condensate and CCN surface
μ_a	Dynamic viscosity of the atmosphere
$\mu_1, \mu_2, \mu_3, \mu_4$	Coefficients for the dynamic viscosity parameterization
n	Number density of condensate vapor molecules
n_k	Number density of particles in size bin k
\mathbf{n}^t	State vector of all gas and particle bin number densities at timestep t
N_A	Avogadro's number
N_s	Surface density of adsorption sites on the CCN
∇_{ad}	Adiabatic temperature gradient, $(\partial \ln T / \partial \ln P)_S$
ν	Attempt frequency for molecular desorption from the CCN
$\nu_{\text{cloud}}^{\text{gas}}$	Stoichiometric ratio of the gas in the condensation reaction
ν_r^{key}	Stoichiometric ratio of the limiting reactant in a Type III reaction

Table 3 *continued on next page*

Table 3 (*continued*)

Symbol	Description
P	Atmospheric pressure
$P_{ijk}^\downarrow, P_{ijk}^\uparrow$	Partition factors distributing a coagulation product between adjacent mass bins
p_i	Equilibrium partial pressure of gas species i
p_i'	Saturation vapor pressure of gas species i
p_s	Saturation vapor pressure of condensate
p_v	Partial pressure of condensate vapor
Φ	Diffusion flux of vapor molecules
r	Radius of a cloud particle
r_m	Mass ratio between adjacent mass bins, $r_m = m_{k+1}/m_k$
r_N	Radius of the cloud condensation nucleus (CCN)
R	Ideal gas constant
R_d	Radial distance from the center of a cloud particle
Re	Reynolds number of a falling particle
ρ_a	Atmospheric mass density
ρ_p	Bulk density of condensed particles
ρ_s	Saturation vapor density at the particle surface
ρ_v	Condensate vapor density
S	Saturation ratio, $S = p_v/p_s$; also the source (production) term in the semi-implicit coagulation/growth update
$S_{\text{het evap}}$	Source term from cores left behind by evaporating heterogeneous particles
S_k	Stokes number; also the production rate into bin k in the semi-implicit update
S_r	Effective supersaturation ratio for Type III reactions, $S_r = S^{1/\nu_r^{\text{key}}}$
σ	Surface tension of the condensate–vapor interface
σ_0, σ_1	Coefficients of the linear surface-tension fit, $\sigma = \sigma_0 + \sigma_1 T$
T	Atmospheric temperature
T_p	Temperature of the cloud particle
u	Advection velocity in the generalized coordinate ξ
v_{ed}	Eddy-diffusion vertical velocity
v_i	Mean thermal speed of particles in bin i
v_t	Terminal (sedimentation) velocity of a particle
v_{winds}	User-specified upward wind speed
v^\uparrow, v^\downarrow	Upward / downward effective velocities across a bin boundary
ξ	Generalized advection coordinate (altitude or particle mass)
Z	Zeldovich factor (non-equilibrium correction to nucleation rate)
Z_{het}	Zeldovich factor for heterogeneous nucleation

B. DEFAULT CARMAPY CONDENSATES

We present here the parameters used for the default CARMAPY condensates in Tables 4 - 13. The indices of refraction for these condensates were taken from the sources in the POSEIDON (R. J. MacDonald & N. Madhusudhan 2017; R. J. MacDonald 2023) opacity database. The individual sources used for each condensate are cited in the respective tables.

Table 4. Physical and Thermodynamic Parameters for KCl Condensate

Symbol	Description	Value	Reference
ρ_p	Condensed Density (g cm^{-3})	1.988	–
M	Molecular Weight	74.5	–
σ_0	Surface Energy (erg cm^{-2})	179.52	G. W. C. Kaye & T. H. Laby (2005)
σ_1	Surface Energy Slope ($\text{erg cm}^{-2} \text{K}^{-1}$)	0.07	
α_0	Saturation Vapor Pressure Offset	7.6106	C. V. Morley et al. (2012)
α_1	SVP Temperature Coefficient (K)	11382	
α_2	SVP Metallicity Coefficient	0	
α_3	SVP Pressure Coefficient	0	
	Condensation Reaction	KCl = KCl [s]	C. V. Morley et al. (2012)
	Key (Limiting) Species	KCl	–
d_q	Collision Diameter (cm)	3.08×10^{-8}	Estimated from R. T. Sanderson (1976)
M_v	Molecular Weight of Limiting Species	74.5	–
	Indices of Refraction	–	H. R. Wakeford & D. K. Sing (2015) E. D. Palik (1985)

Table 5. Physical and Thermodynamic Parameters for ZnS Condensate

Symbol	Description	Value	Reference
ρ_p	Condensed Density (g cm^{-3})	4.04	–
M	Molecular Weight	97.474	–
σ_0	Surface Energy (erg cm^{-2})	860	H. Zhang et al. (2003)
σ_1	Surface Energy Slope ($\text{erg cm}^{-2} \text{K}^{-1}$)	0	
α_0	Saturation Vapor Pressure Offset	12.812	C. V. Morley et al. (2012)
α_1	SVP Temperature Coefficient (K)	15873	
α_2	SVP Metallicity Coefficient	1	
α_3	SVP Pressure Coefficient	0	
	Condensation Reaction	$\text{H}_2\text{S} + \text{Zn} = \text{ZnS[s]}$	C. V. Morley et al. (2012)
	Key (Limiting) Species	Zn	–
d_q	Collision Diameter (cm)	3.67×10^{-8}	Estimated from L. N. Zack & L. M. Ziurys (2009)
M_v	Molecular Weight of Limiting Species	65.38	–
	Indices of Refraction	–	H. R. Wakeford & D. K. Sing (2015) M. R. Querry (1987)

Table 6. Physical and Thermodynamic Parameters for Na₂S Condensate

Symbol	Description	Value	Reference
ρ_p	Condensed Density (g cm ⁻³)	1.856	–
M	Molecular Weight	78.0452	–
σ_0	Surface Energy (erg cm ⁻²)	1033	E. Lee (priv. comm.)
σ_1	Surface Energy Slope (erg cm ⁻² K ⁻¹)	0	
α_0	Saturation Vapor Pressure Offset	8.55	C. V. Morley et al. (2012)
α_1	SVP Temperature Coefficient (K)	13889	
α_2	SVP Metallicity Coefficient	0.5	
α_3	SVP Pressure Coefficient	0	
	Condensation Reaction	H ₂ S + 2Na = Na ₂ S[s] + H ₂	C. V. Morley et al. (2012)
	Key (Limiting) Species	Na	–
			Estimated from
d_q	Collision Diameter (cm)	4.2×10^{-8}	L. Glasser & H. D. B. Jenkins (2000)
M_v	Molecular Weight of Limiting Species	22.9898	–
			H. R. Wakeford & D. K. Sing (2015), C. V. Morley et al. (2012), A. Montaner et al. (1979), H. Khachai et al. (2009)
	Indices of Refraction	–	

Table 7. Physical and Thermodynamic Parameters for MnS Condensate

Symbol	Description	Value	Reference
ρ_p	Condensed Density (g cm ⁻³)	4.0	–
M	Molecular Weight	87.003	–
σ_0	Surface Energy (erg cm ⁻²)	2326	E. Lee (priv. comm.)
σ_1	Surface Energy Slope (erg cm ⁻² K ⁻¹)	0	
α_0	Saturation Vapor Pressure Offset	11.532	C. V. Morley et al. (2012)
α_1	SVP Temperature Coefficient (K)	23810	
α_2	SVP Metallicity Coefficient	1	
α_3	SVP Pressure Coefficient	0	
	Condensation Reaction	H ₂ S + 2Mn = Mn ₂ S[s] + H ₂	C. V. Morley et al. (2012)
	Key (Limiting) Species	Mn	–
			Estimated from
d_q	Collision Diameter (cm)	3.68×10^{-8}	C. B. Honsberg & S. G. Bowden (2007)
M_v	Molecular Weight of Limiting Species	54.938	–
			D. Kitzmann & K. Heng (2018), A. Montaner et al. (1979), D. R. Huffman & R. L. Wild (1967)
	Indices of Refraction	–	

Table 8. Physical and Thermodynamic Parameters for Cr Condensate

Symbol	Description	Value	Reference
ρ_p	Condensed Density (g cm^{-3})	7.15	–
M	Molecular Weight	51.9961	–
σ_0	Surface Energy (erg cm^{-2})	2068.63	G. W. C. Kaye & T. H. Laby (2005)
σ_1	Surface Energy Slope ($\text{erg cm}^{-2} \text{K}^{-1}$)	0.2	
α_0	Saturation Vapor Pressure Offset	7.49	C. V. Morley et al. (2012)
α_1	SVP Temperature Coefficient (K)	20592	
α_2	SVP Metallicity Coefficient	0	
α_3	SVP Pressure Coefficient	0	
	Condensation Reaction	Cr = Cr[s]	C. V. Morley et al. (2012)
	Key (Limiting) Species	Cr	–
d_q	Collision Diameter (cm)	3.66×10^{-8}	Atomic Radius
M_v	Molecular Weight of Limiting Species	51.9961	–
			D. Kitzmann & K. Heng (2018), D. Lynch & W. R. Hunter (1997), A. D. Rakic et al. (1998)
	Indices of Refraction	–	

Table 9. Physical and Thermodynamic Parameters for Mg_2SiO_4 Condensate

Symbol	Description	Value	Reference
ρ_p	Condensed Density (g cm^{-3})	3.21	–
M	Molecular Weight	140.69	–
σ_0	Surface Energy (erg cm^{-2})	436	T. Kozasa et al. (1989)
σ_1	Surface Energy Slope ($\text{erg cm}^{-2} \text{K}^{-1}$)	0	
α_0	Saturation Vapor Pressure Offset	14.88	C. Visscher (priv. comm.)
α_1	SVP Temperature Coefficient (K)	32488	
α_2	SVP Metallicity Coefficient	1.4	
α_3	SVP Pressure Coefficient	0.2	
	Condensation Reaction	$2\text{Mg} + \text{SiO} + 3\text{H}_2\text{O}$ $= \text{Mg}_2\text{SiO}_4[\text{s}] + 3\text{H}_2$	C. Helling & P. Woitke (2006)
	Key (Limiting) Species	Mg	–
d_q	Collision Diameter (cm)	3.85×10^{-8}	Estimated from L. Glasser & H. D. B. Jenkins (2000)
M_v	Molecular Weight of Limiting Species	24.305	–
			B. Burningham et al. (2021), C. Jäger et al. (2003)
	Indices of Refraction	–	

Table 10. Physical and Thermodynamic Parameters for Fe Condensate

Symbol	Description	Value	Reference
ρ_p	Condensed Density (g cm^{-3})	7.87	–
M	Molecular Weight	55.845	–
σ_0	Surface Energy (erg cm^{-2})	2565.2285	G. W. C. Kaye & T. H. Laby (2005)
σ_1	Surface Energy Slope ($\text{erg cm}^{-2} \text{K}^{-1}$)	0.39	
α_0	Saturation Vapor Pressure Offset	7.23	C. Visscher et al. (2006)
α_1	SVP Temperature Coefficient (K)	20995	
α_2	SVP Metallicity Coefficient	0	
α_3	SVP Pressure Coefficient	0	
	Condensation Reaction	Fe = Fe[s]	C. Helling & P. Woitke (2006)
	Key (Limiting) Species	Fe	–
d_q	Collision Diameter (cm)	3.7×10^{-8}	Atomic Radius
M_v	Molecular Weight of Limiting Species	55.845	–
			D. Kitzmann & K. Heng (2018), D. Lynch & W. R. Hunter (1997)
	Indices of Refraction	–	

Table 11. Physical and Thermodynamic Parameters for TiO₂ Condensate

Symbol	Description	Value	Reference
ρ_p	Condensed Density (g cm^{-3})	4.25	–
M	Molecular Weight	79.866	–
σ_0	Surface Energy (erg cm^{-2})	535.124	E. Lee et al. (2015)
σ_1	Surface Energy Slope ($\text{erg cm}^{-2} \text{K}^{-1}$)	0.04396	
α_0	Saturation Vapor Pressure Offset	9.5489	C. Helling et al. (2001)
α_1	SVP Temperature Coefficient (K)	32456.8678	
α_2	SVP Metallicity Coefficient	0	
α_3	SVP Pressure Coefficient	0	
	Condensation Reaction	TiO ₂ = TiO ₂ [s]	C. Helling & P. Woitke (2006)
	Key (Limiting) Species	TiO ₂	–
			Estimated from
d_q	Collision Diameter (cm)	3.39×10^{-8}	C. Helling et al. (2001)
M_v	Molecular Weight of Limiting Species	79.866	–
			E. K. H. Lee et al. (2022), M. W. Ribarsky (1997), S. Zeidler et al. (2011)
	Indices of Refraction	–	

Table 12. Physical and Thermodynamic Parameters for Al₂O₃ Condensate

Symbol	Description	Value	Reference
ρ_p	Condensed Density (g cm ⁻³)	3.99	–
M	Molecular Weight	101.96	–
σ_0	Surface Energy (erg cm ⁻²)	690	T. Kozasa et al. (1989)
σ_1	Surface Energy Slope (erg cm ⁻² K ⁻¹)	0	
α_0	Saturation Vapor Pressure Offset	17.7	H. R. Wakeford et al. (2017)
α_1	SVP Temperature Coefficient (K)	45892.6	
α_2	SVP Metallicity Coefficient	1.66	
α_3	SVP Pressure Coefficient	0	
	Condensation Reaction	2Al + 3H ₂ O = Al ₂ O ₃ + 3H ₂	E. Sedlmayr & H.-P. Gail (2014).
	Key (Limiting) Species	Al	–
			Estimated From
d_q	Collision Diameter (cm)	3.83×10^{-8}	E. R. Dobrovinskaya et al. (2009)
M_v	Molecular Weight of Limiting Species	26.98	–
			D. Kitzmann & K. Heng (2018), B. Begemann et al. (1997), C. Koike et al. (1995)
	Indices of Refraction	–	

Table 13. Physical and Thermodynamic Parameters for SiO Condensate

Symbol	Description	Value	Reference
ρ_p	Condensed Density (g cm ⁻³)	2.13	–
M	Molecular Weight	44.0849	–
σ_0	Surface Energy (erg cm ⁻²)	500	E. Sedlmayr & H.-P. Gail (2014)
σ_1	Surface Energy Slope (erg cm ⁻² K ⁻¹)	0	
α_0	Saturation Vapor Pressure Offset	14.12	H.-P. Gail et al. (2013)
α_1	SVP Temperature Coefficient (K)	21506.3	
α_2	SVP Metallicity Coefficient	0	
α_3	SVP Pressure Coefficient	0	
	Condensation Reaction	SiO = SiO[s]	E. Sedlmayr & H.-P. Gail (2014)
	Key (Limiting) Species	SiO	–
			Estimated from
d_q	Collision Diameter (cm)	4.4×10^{-8}	E. Sedlmayr & H.-P. Gail (2014)
M_v	Molecular Weight of Limiting Species	44.0849	–
			D. Kitzmann & K. Heng (2018), H. R. Phillip (1997), S. Wetzel et al. (2013)
	Indices of Refraction	–	